J. Fluid Mech. (1995), *vol.* 296, *pp.* 39–71

Head-on collision of two coaxial vortex rings: experiment and computation

By CHIN-CHOU CHU, CHI-TZUNG WANG,
CHIEN-CHENG CHANG, RAY-YU CHANG
AND WEN-TYZH CHANG

Institute of Applied Mechanics, College of Engineering, National Taiwan University, Taipei 106,
Taiwan, Republic of China

(Received 11 March 1993 and in revised form 4 January 1995)

Head-on collision of two coaxial vortex rings has been studied by joint experimental and numerical investigation. The Reynolds number, Re_{Γ}, based on the initial circulation of the vortex rings, ranged from 400 to 2700. Besides numerical data, the vorticity field was also resolved by a non-intrusive visualization technique, LIPA, which enabled simultaneous measurement of velocities at multiple locations on a plane area. It was found that the enstrophy, rather than circulation, revealed three stages of evolution of the vortex rings prior to their breakdown. These include the free-travelling stage, stage of vortex stretching and the stage of viscous dissipation dominance. The results indicate that it would be incorrect to neglect the viscous effect, in particular, for the latter two stages of flow development. In fact, the rebound behaviour of the vortex rings for lower Re_{Γ} is essentially a viscous phenomenon and is found to be closely related to the dissipation of enstrophy when the vortex rings are brought to interact actively with each other and is also related to the increase of the vorticity core diameter in the stage of dominance of viscous dissipation. Furthermore, an instant dimensionless group, N_t/Re_{Γ}, based on the local vorticity distribution and the radius of a vortex ring, is found to be appropriate to characterize the onset of instability. Our investigation indicates that, in the range of observation, bulging instability will be observed during collision when N_t/Re_{Γ} exceeds a critical value, $(N_t/Re_{\Gamma})_{cr}$, which is a function of the initial core-size of the vortex ring. Comparisons showed that the numerical, measured, and visualization results were in consistent agreement; this not only enables us to assess the range of validity of the axisymmetry assumed for the numerical simulation, but also provides us with a rational basis for further analysis of azimuthal instability.

1. Introduction

Vortex rings have been a subject of interest in vortex dynamics because of a plethora of physical phenomena revealed by their motions and interactions with a boundary. The review article by Shariff & Leonard (1992) shows the rich variety of research in vortex rings, encompassing analytical, numerical and experimental results. In the present study, we are concerned with the problem of head-on collision of two coaxial vortex rings of opposite senses of rotation (see figure 1). In her visualization study, Oshima (1978) observed that the smoke cross-sections of vortex rings deform from a circular to a head with a long trailing tail during the collision; subsequently, the head pinches off from the tail and continually increases in radius. At larger radii, azimuthal waviness pinches to form a dozen or so smaller rings. Kambe and his coworkers (Kambe & Minota 1983; Kambe & Mya Oo 1984) studied head-on collision by

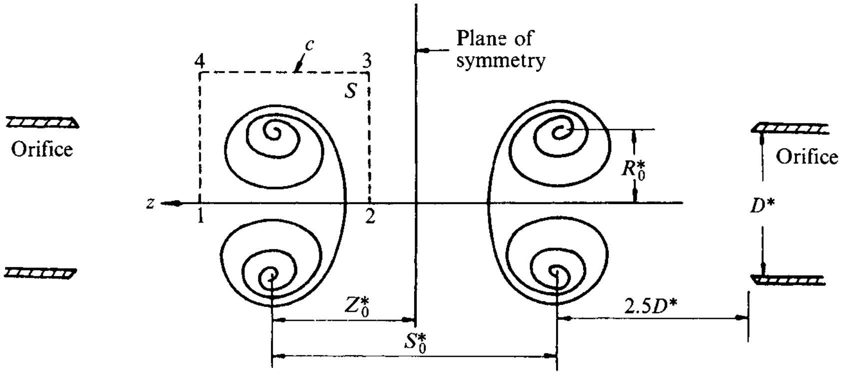

FIGURE 1. The meridian cross-section of the physical problem and the definition of various lengthscales.

numerical simulation, primarily to test theories of vortex sound generation. These authors indicated that the viscous effect is important during collision. On the other hand, Shariff *et al.* (1988), using contour dynamics, revealed some of the inviscid effects of head-on collisions of vortex rings and suggested that inviscid core deformation was sufficient for acoustic emission. Stanaway, Shariff & Hussain (1988) carried out a numerical study of the head-on collision of two vortex rings. They considered two different rings: one was a thin-core vortex ring with Gaussian distribution, and the other was a smoothed Hill's vortex using direct simulations of the incompressible Navier–Stokes equations. Recently, Lim & Nickels (1992) used coloured dye to reveal the detailed structure of the small rings and several other features, including short-wavelength instability around the circumference of the colliding rings and a turbulent cloud with occasional appearance of small rings. Apparently, their experimental results indicate that the viscous effect plays a role during the process of interaction of the vortex rings. Unfortunately, the previous experimental results did not provide quantitative unsteady data such as for velocity and vorticity; it is, therefore, unclear under which conditions and to what extent the viscous effect is significant for the behaviours of the vortex rings during head-on collision. A satisfactory answer to this problem needs further experimental and numerical clarification.

The present study is guided by flow visualization and will be restricted to the stages before the flow is unstable and becomes fully three-dimensional. In particular, we examine the possibility of rebound of the vortex rings, which is a strong indication of the viscous effect. Peace & Riley (1983) studied the rebound behaviour for a pair of line vortices approaching a stress-free plane boundary as well as a no-slip plane boundary and concluded that rebound is essentially a viscous phenomenon. However, there is no stretching effect in two space dimensions, and the effect has to be incorporated in the motion of vortex rings. Prior to azimuthal instability, the vortex rings are quite symmetric about their common axis, for which numerical analysis and quantitative measurement is carried out. The measurement is performed by the technique LIPA (laser induced photochemical anemometry) for measuring the velocity (vorticity) field. The technique enables simultaneous measurement of velocities at multiple locations on a planar area. This feature is of particular importance in understanding unsteady flows, and the technique has demonstrated some success for flow past a cylinder and for vortex rings impinging on planar surfaces (cf. Chu & Liao 1992; Chu, Wang & Hsieh 1993). In order to have meaningful comparison between numerical and experimental results, the vorticity field is measured by LIPA after the vortex rings are well developed

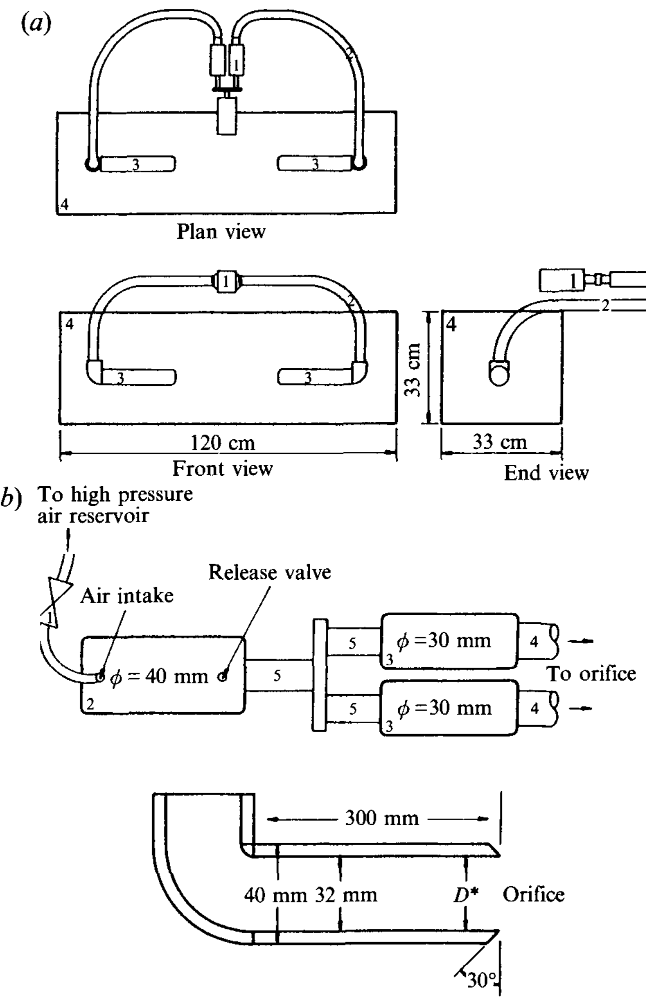

FIGURE 2. (*a*) A sketch of the experimental apparatus; 1. Dual parallel piston system; 2. PVC tubing; 3. Vortex ring generating orifice; 4. Water or kerosene tank. (*b*) a detailed sketch of the vortex-ring-generating system; 1. Electromagnetic valve; 2. Pneumatic driving piston; 3. Dual parallel driven pistons; 4. PVC tubing; 5. Rigid connector.

at 2.5 times the orifice diameter downstream of the generator. Finite-core assumptions based on the measured data served as the initial conditions for numerical simulation under the assumption of axisymmetric flow. Results will be presented for several trajectories associated with the vortex rings, contours of vorticity, circulation and the time variation of the total enstrophy along with its production and dissipation, a mechanism for the rebound of a vortex ring, and a criterion of bulging instability around the circumference of vortex rings.

2. Numerical simulation

2.1. *Governing equations*

Refer to figure 1. The flow considered is that induced by a vortex ring with initial circulation Γ_0^* and initial radius R_0^* in the presence of a stress-free plane boundary

$z = 0$, where R_0^* is the distance between the vorticity centre of the ring core and the flow axis. The flow is assumed to be axisymmetric and incompressible with constant density and viscosity. The vorticity ω thus contains only the azimuthal component, and with reference to the cylindrical coordinates, the Stokes streamfunction ψ can be introduced such that

$$u_r = -\frac{1}{r}\frac{\partial \psi}{\partial z}, \quad u_z = \frac{1}{r}\frac{\partial \psi}{\partial r}, \tag{2.1}$$

where u_r, u_z denote the velocity components. The governing equation can be written as

$$\frac{\partial \omega}{\partial t} + u_r \frac{\partial \omega}{\partial r} + u_z \frac{\partial \omega}{\partial z} = \frac{\omega}{r} u_r + \frac{1}{Re_\Gamma}\left(\frac{\partial^2 \omega}{\partial r^2} + \frac{1}{r}\frac{\partial \omega}{\partial r} - \frac{\omega}{r^2} + \frac{\partial^2 \omega}{\partial z^2}\right), \tag{2.2}$$

$$\frac{\partial}{\partial r}\left(\frac{1}{r}\frac{\partial \psi}{\partial r}\right) + \frac{1}{r}\frac{\partial^2 \psi}{\partial z^2} = -\omega. \tag{2.3}$$

Equations (2.1)–(2.3) are cast in dimensionless form. The characteristic length, velocity, and vorticity are taken respectively to be R_0^*, Γ_0^*/R_0^* and Γ_0^*/R_0^{*2}, while $Re_\Gamma = \Gamma_0^*/\nu$ is the Reynolds number with ν the kinematic viscosity of the fluid. The initial vortex centre is then $(1, \pm z_0)$.

The boundary conditions satisfied by the streamfunction ψ and vorticity ω are: (i) $\psi(r, 0) = 0$, and $\psi(r, z) \rightarrow 0$, as $(r^2 + z^2)^{1/2} \rightarrow \infty$; (ii) the stress-free boundary condition $\omega(r, 0) = 0$, and far-field condition $\omega(r, z) \rightarrow 0$, as $(r^2 + z^2)^{1/2} \rightarrow \infty$.

2.2. *Numerical method*

Both the vorticity equation and the Poisson equation for the streamfunction are solved by using the SOR (successive-over-relaxation) scheme. Substituting (2.1) into (2.2) yields

$$\frac{\partial \omega}{\partial t} + \frac{\partial}{\partial r}\left(-\frac{1}{r}\frac{\partial \psi}{\partial z}\omega\right) + \frac{\partial}{\partial z}\left(\frac{1}{r}\frac{\partial \psi}{\partial r}\omega\right) = \frac{1}{Re_\Gamma}\left(\frac{\partial^2 \omega}{\partial r^2} + \frac{1}{r}\frac{\partial \omega}{\partial r} - \frac{\omega}{r^2} + \frac{\partial^2 \omega}{\partial z^2}\right). \tag{2.4}$$

It is this equation together with (2.3) to which the numerical scheme is applied to continue the solution. The computational domain is of $[0, W] \times [0, H]$, in which $(N+1) \times (M+1)$ grid points are distributed.

The grid distribution in the r-direction is of the form $r(X) = a_1 X + a_2 X^7$ in order to make sure that the grid spacing near the axis ($r = 0$) is uniform and small enough while the mesh in the z-direction is determined by a polynomial of order 5,

$$z(Y) = b_1 Y + b_2 Y^2 + \ldots + b_5 Y^5,$$

in order to have a dense distribution near the vortex centre as well as the colliding surface. The coefficients a_1 and a_2 are determined by: (i) $r(N) = W$; (ii) the requirement that about 80% of the grid points in the r-direction be inside half the domain $[0, \frac{1}{2}W]$. The coefficients $(b_1, \ldots, b_5)$ are determined from the following conditions: (i) the grid spacing at $z = 0$ is $2(\Delta t/Re_\Gamma)^{1/2}$, where Δt is the timestep; (ii) $z(M) = H$; (iii) 60% of the grid points in the z-direction are inside $[0, z_0]$; (iv) the grid spacing at the initial vortex centre ($z = z_0$) is of size $4(\Delta t/Re_\Gamma)^{1/2}$; (v) the grid points are most dense at the initial vortex centre and along the colliding surface.

With the grid distribution $r = r(X), z = z(Y)$, (2.4) and (2.3) can be rewritten as

$$\frac{\partial \omega}{\partial t} = pq\left[\frac{\partial}{\partial X}\left(\frac{1}{r}\frac{\partial \psi}{\partial Y}\omega\right) - \frac{\partial}{\partial Y}\left(\frac{1}{r}\frac{\partial \psi}{\partial X}\omega\right)\right] + \frac{1}{Re_\Gamma}\left[p^2\frac{\partial^2 \omega}{\partial X^2} + \left(-p^3\alpha + \frac{p}{r}\right)\frac{\partial \omega}{\partial X} - \frac{\omega}{r^2} + q^2\frac{\partial^2 \omega}{\partial Y^2} - q^3\beta\frac{\partial \omega}{\partial Y}\right], \tag{2.5}$$

$$-r\omega = p^2\frac{\partial^2 \psi}{\partial X^2} - \left(p^3\alpha + \frac{p}{r}\right)\frac{\partial \psi}{\partial X} + q^2\frac{\partial^2 \psi}{\partial Y^2} - q^3\beta\frac{\partial \psi}{\partial Y}, \tag{2.6}$$

where

$$\begin{cases} p(X) = \left(\dfrac{\mathrm{d}r}{\mathrm{d}X}\right)^{-1}, \\ q(Y) = \left(\dfrac{\mathrm{d}z}{\mathrm{d}Y}\right)^{-1}, \end{cases} \quad \begin{cases} \alpha(X) = \dfrac{\mathrm{d}^2 r}{\mathrm{d}X^2}, \\ \beta(Y) = \dfrac{\mathrm{d}^2 z}{\mathrm{d}Y^2}. \end{cases}$$

Central difference approximation is then applied to obtain the difference representations of the above equations, which are

$$\frac{\partial \omega}{\partial t} \approx A(\psi, \omega)$$

$$= a_{i,j}\,\omega_{i-1,j} + b_{i,j}\,\omega_{i+1,j} + c_{i,j}\,\omega_{i,j} + d_{i,j}\,\omega_{i,j-1} + e_{i,j}\,\omega_{i,j+1}, \tag{2.7}$$

$$-r_i\,\omega_{i,j} = \bar{a}_{i,j}\,\psi_{i-1,j} + \bar{b}_{i,j}\,\psi_{i+1,j} + \bar{c}_{i,j}\,\psi_{i,j} + \bar{d}_{i,j}\,\psi_{i,j-1} + \bar{e}_{i,j}\,\psi_{i,j+1}. \tag{2.8}$$

With vorticity field ω^n given at timestep t_n, the streamfunction can be found by solving (2.8). The convergence of solving the streamfunction in the SOR scheme is checked by comparing the maximum norm of the difference of $\psi_{i,j}$ in two successive iterations with the value of ϵ_f, which is of order 10^{-6} in the present study. The vorticity field ω^{n+1} at the next timestep is obtained by solving the following equation:

$$\frac{\omega^{n+1} - \omega^n}{\Delta t} = \tfrac{1}{2}[A(\psi^{n+1}, \omega^{n+1}) + A(\psi^n, \omega^n)]. \tag{2.9}$$

The procedure is as follows: (i) denote the value of ω^{n+1} at the jth iteration by $\omega^{n+1}_{(j)}$ with $\omega^{n+1}_{(0)} = \omega^n$; (ii) solve (2.8) to obtain $\psi^{n+1}_{(j)}$ and update the value of $\omega^{n+1}_{(j)}$ at the boundary; (iii) obtain $\omega^{n+1}_{(j+1)}$ by solving (2.9) with ω^{n+1} substituted by $\omega^{n+1}_{(j)}$, and ψ^{n+1} by $\psi^{n+1}_{(j)}$; (iv) check the convergence of $\omega^{n+1}_{(j+1)}$ by comparing the maximum norm of $|\omega^{n+1}_{(j+1)} - \omega^{n+1}_{(j)}|$ with the value set by ϵ_ω, which is of order 10^{-5}; if the convergence condition is not satisfied, repeat (ii)–(iii).

3. Experimental details

3.1. *Experimental apparatus*

Experiments were carried out in a glass tank which was 120 cm long, 33 cm wide, and 33 cm high with water or kerosene as the working fluid for qualitative and quantitative investigation, respectively. The experimental apparatus is shown schematically in figure 2, and consisted of a vortex ring generating system and a control system. The vortex ring generating system, shown in figure 2(*b*), included a pair of parallel pistons and sharp-edged orifices.

This pair of parallel pistons was rigidly connected to a pneumatic piston-and-cylinder, which was powered by high-pressure compressed air. Each of the pistons was connected to a sharp-edged orifice by PVC tubing filled with the working fluid. The stroke of the pneumatic cylinder was fixed at 1.5 cm, and the speed of the motion of the piston was varied from 3.5 to 6.4 cm s^{-1}, depending on the released pressure of the exit valve on the pneumatic piston-and-cylinder. When the electromagnetic valve was energized, the high-pressure air pushed the piston to move at a constant speed in the cylinder, driving the pair of pistons synchronously. As the pistons moved, a slug of fluid was released from each of the orifices and rolled up into vortex rings moving towards each other in a common axis. For each size of vortex ring generator, there were three parameters in the vortex-ring-generating system that affected the Reynolds number of the vortex ring: the inner diameter of the piston-and-cylinder, the stroke of the piston, and the speed of the piston. In the present study, the dimensions of the piston and the stroke of the piston were fixed, and the speed of the piston was the only parameter that could be varied to generate the vortex ring at different Reynolds numbers for each size of orifice. In order to have a thorough investigation on azimuthal instability, three sizes of inner diameter of the orifice were used for experiment, which were 38 mm, 32 mm and 23.5 mm. The distance between the exits of two orifices was also varied from six to twelve times the orifice diameter.

3.2. *Experimental methods*

3.2.1. *Flow visualization by dye-injection*

The flow visualization of the global phenomena was performed in a water tank. The vortex rings were made visible by neutrally buoyant dyes in each of the vortex-ring generators. Blue and red food colours were pre-injected into each of the vortex-ring generators, respectively. Once the discoloured fluids were pushed out of the exit of the generator by pistons, two vortex rings which were of different colours were formed which enabled us to visualize the global phenomena during the collision process. Visual data were recorded on Kodak 100 negative film using a Nikon F-3 camera with a motor drive or a Photosonics 35 mm movie camera.

3.2.2. *Laser-induced photochemical anemometry* (*LIPA*)

Laser induced photochemical anemometry (LIPA) is a non-intrusive optical technique which enables simultaneous measurement of unsteady velocities at multiple locations on a planar flow area. The historical review of LIPA was given by Chu & Liao (1992). When a photochromic chemical is added into a fluid and is homogeneously dispersed, a grid of pulsed laser beams passing through the doped fluid results in a colour change along the beams because of the phenomenon of photochromism. The excitation time of the chemical is long, compared with the timescale of the flow. Thus, the discoloured grid consists of timelines which contain fluid material of fixed identity. As the fluid continues to move, the grid, marked by the colour, will have significant distortion during the excitation time of the chemical. Only two images are needed to calculate the flow information from the motion of each intersection point over the grid area. The chemical added to the fluid in the current study was 8 p.p.m. of Kodak long-time photochromic chemical (1,3-trimethyl-8-nitrospiro [2-H-1-benzopyran-2,2′-indoline]). The working fluid was deodorized kerosene (FC-180). The UV light source was a Lambda Physik LPX-200 excimer laser running on XeF with approximately 150 mJ output and a 20 ns pulse duration with an adjustable repetition rate from 1 to 100 Hz.

3.2.3. *Flow visualization by photochromic timelines*

Flow patterns can be visualized by the generation of photochromic timelines in the meridian plane of each vortex ring before collision. Thus, the rolling-up of the timeline marks in each of the vortex rings can be clearly observed during the collision process. Figure 3(*a*) shows a sketch of the optical set-up of the photochromic timeline visualization. The repetition rate was set at 40 Hz, and the images were recorded by a Nikon F-3 camera on Kodak 100 film.

3.2.4. *Large-field measurement*

Figure 3(*b*) shows a schematic drawing of the LIPA set-up used to obtain the large-field information. Figure 4 shows two photos of an LIPA grid and its distortion as the fluid moves. The grid lines are about 150 μm wide, and the mesh size is about 2 mm square. Because the history of each specific grid point is known, we are able to compute the velocity according to the displacement of each grid point, deduced from the two photographs shown in figure 4. The details of the procedure for conversion of displacement to velocity at each grid point, the calculation of circulation and vorticity associated with a small area surrounded by four adjacent grid points, and the analysis of uncertainty in estimating vorticity from the measured velocities have also been presented by Chu & Liao (1992).

The large-field measurements in the present study were limited to the axisymmetric cases before the appearance of azimuthal instability of the vortex ring. The initial vorticity distribution of a vortex ring as well as its dependence on the dimension of the orifice and the Reynolds number were obtained by using this method. In each run of the experiment, the measuring area was adjusted to cover the region of interest in the meridian plane according to the result of flow visualization at different times. A total of three to five locations were chosen to obtain the large-field information before and after collision. The criterion to examine whether a set of data is qualified to reconstruct the unsteady flow information was based on the initial Reynolds number. During the large-field measurement, we simultaneously monitored the Reynolds number at the location where the initial condition of the vortex ring was determined. Therefore, a set of data was acceptable provided the initial Reynolds number of the vortex ring varied less than 4% from the pre-set value. For each measurement location, at least three sets of qualified data were collected to examine the repeatability as well as calculate the average circulation and enstrophy. Before the collision, the values of the qualified data were usually within a 5% variation of the mean value.

The sequence of the experimental procedures, timing of image recordings, and time delays of the stroboscope were synchronized by an IBM personal computer. The images were recorded on Kodak 2415 Technical pan film by a Photosonics 35-4ML cine camera or a Nikon F-3 camera with a motor drive. The films were magnified and digitized by an NAC film motion analyser with a spatial resolution of 0.02 mm. The reading error in locating the centre of each intersection point was about 8%, based on the width of the grid line. Thus, the uncertainty of the estimated vorticity was ± 1.5/s in the present study, according to Chu & Liao (1992).

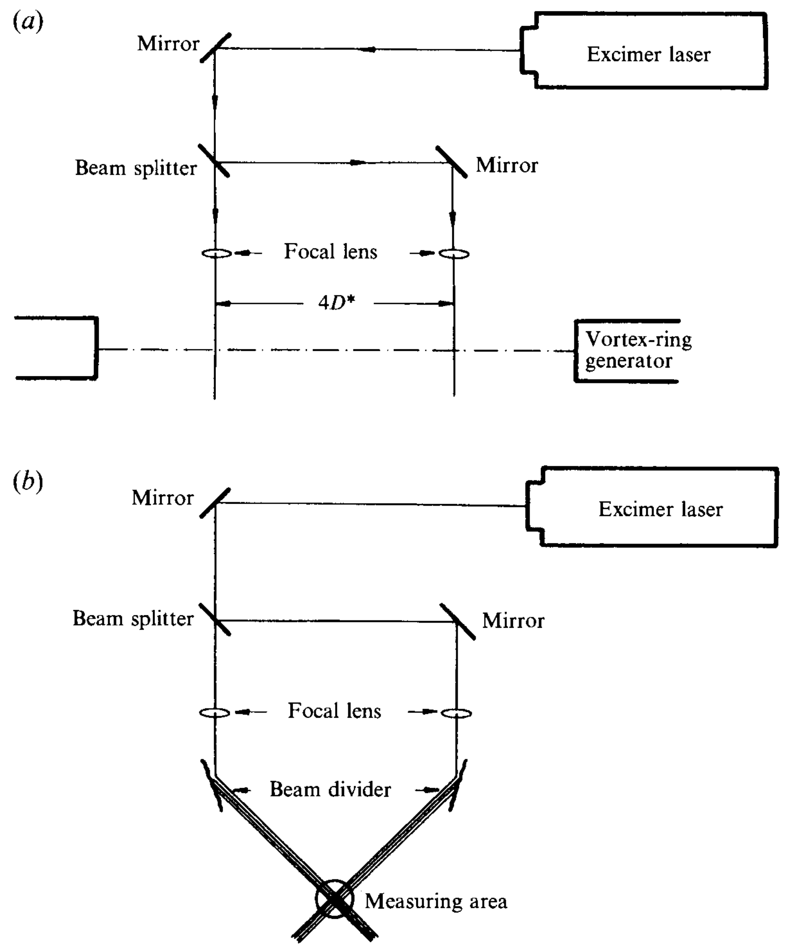

FIGURE 3. (*a*) Optical set-up of the flow visualization generated by photochromic timelines; (*b*) optical set-up used to generate a grid of laser beams over a planar area.

4. Results and discussion

4.1. *Initial conditions*

The visual information indicates that the vortex ring was fully formed at a distance of 2.5 times the orifice diameter downstream of the orifice exit, which was designated as the initial location of the vortex ring, Z_0^* (see figure 1 for definition). Therefore, the associated information including the initial radius, R_0^*, circulation, Reynolds number, and vorticity distribution at the initial location was counted as the initial conditions of a vortex ring for both experiment and calculation. In both dye-injection flow visualization and photochromic timeline visualization, we were able to estimate the vortex ring diameter, $2R_0^*$ (see figure 1 for definition), and its translational speed, U^*, and then calculate the Reynolds number by the definition $Re = 2U^*R_0^*/\nu$. The uncertainty in calculating Re was about 4% in the range of study. Actually, the vortex ring slows down gradually after it is completely formed while the vortex ring diameter increases gradually because of viscous diffusion. Therefore, Re changes slightly before head-on collision. Using the large-field measurement, we were able to estimate the circulation, Γ_0^*, so that the Reynolds number, $Re_\Gamma = \Gamma_0^*/\nu$, could be determined. The

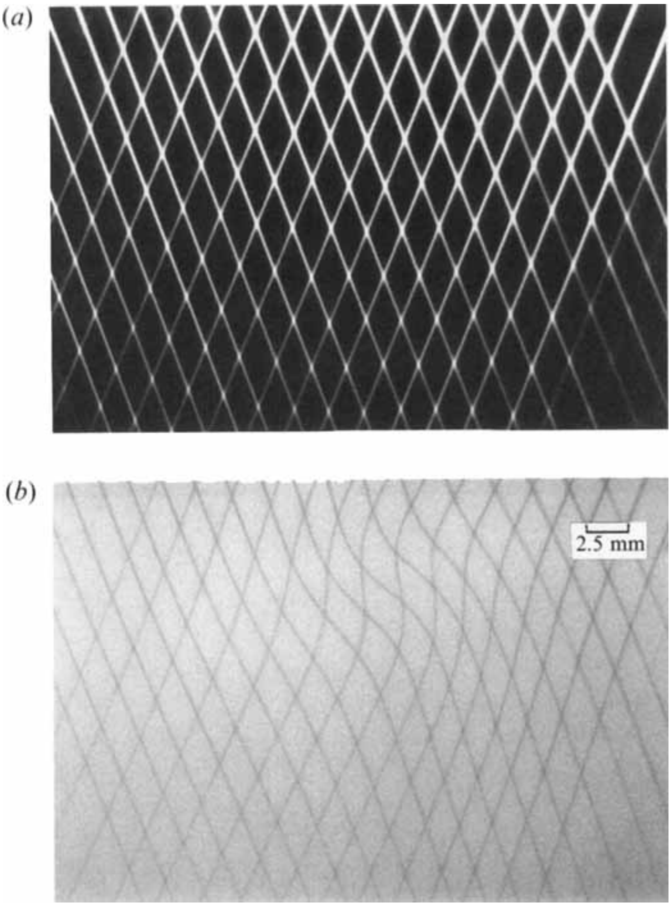

FIGURE 4. Two photographs showing the LIPA grid used to measure the large field information; (*a*) the laser grid; (*b*) 25 ms later.

initial radius of a vortex ring, R_0^*, is defined as the distance between the dyed centre and the flow axis in the meridian cross-section by flow visualization at its initial location. According to the present result, the relationship between the Reynolds numbers obtained by flow visualization (Re) and those of large-field measurement (Re_Γ) can be approximately expressed as $Re_\Gamma \approx 2.1 Re$ in the range of observation regardless of the dimension of the orifice, which is very similar to the result obtained by Chu *et al.* (1993).

Results of large-field measurement show that the initial vorticity distribution in the core region of a vortex ring can be approximately represented by a finite core, $\operatorname{sech}^2(s/c_0)$, where s is the dimensionless distance from vortex centre and the dimensionless core-size, c_0, depends on the Reynolds number and the value of orifice-diameter to piston-stroke ratio, D/L. The value of c_0 was calculated by curve-fitting 25 data points uniformly taken from the two mutually perpendicular axes at the centre of the initial vorticity contours in the region of $s < 0.5$. Figure 8(*a*) shows the corresponding values of c_0 for various Re_Γ as well as various values of D/L. Note that the open circles shown in the figure are the measured data points for c_0 while the respective uncertainty for Re_Γ and c_0 are also presented. In the present study, the stroke of the generating system was fixed. Thus, for a fixed Re_Γ, the relationship between the

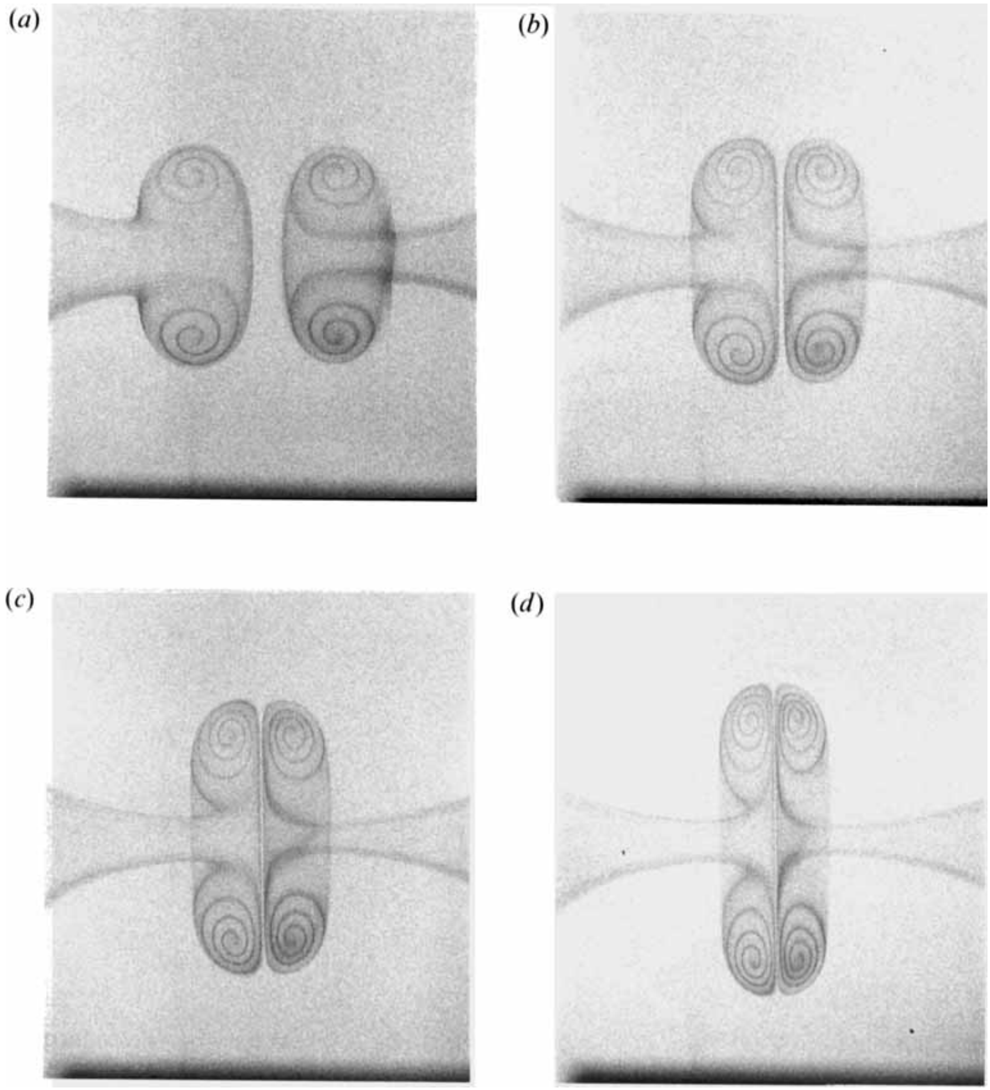

FIGURE 5 (*a–d*). For caption see facing page.

core-size, c_0, and the dimension of the orifice is quite apparent, that is, a vortex ring with more concentrated vorticity distribution will be obtained by a larger orifice.

4.2. *Scope of present study*

Experimental flow visualization was carried out in the range from $Re \approx 400$ to 1300 (i.e. $Re_\Gamma \approx 850$ to 2700) while the initial separation of two vortex rings, $s_0 = S_0^*/R_0^* = 2Z_0^*/R_0^*$, was set to be from four to ten (see figure 1). Numerical calculations were performed for Re_Γ between 400 and 2500. The initial conditions of calculation were provided according to those shown in figure 8(*a*). The value of s_0 was set to be 4, 6 and 8, respectively, while the value of c_0 was chosen between 0.12 and 0.25. The calculated result as well as those obtained by experiment will be presented in the following sections in dimensionless form. Recall that the spatial coordinates r and z are in dimensionless form normalized by the initial radius of a vortex ring, R_0^*. It is found that 200×180 grid points distributed in the computational

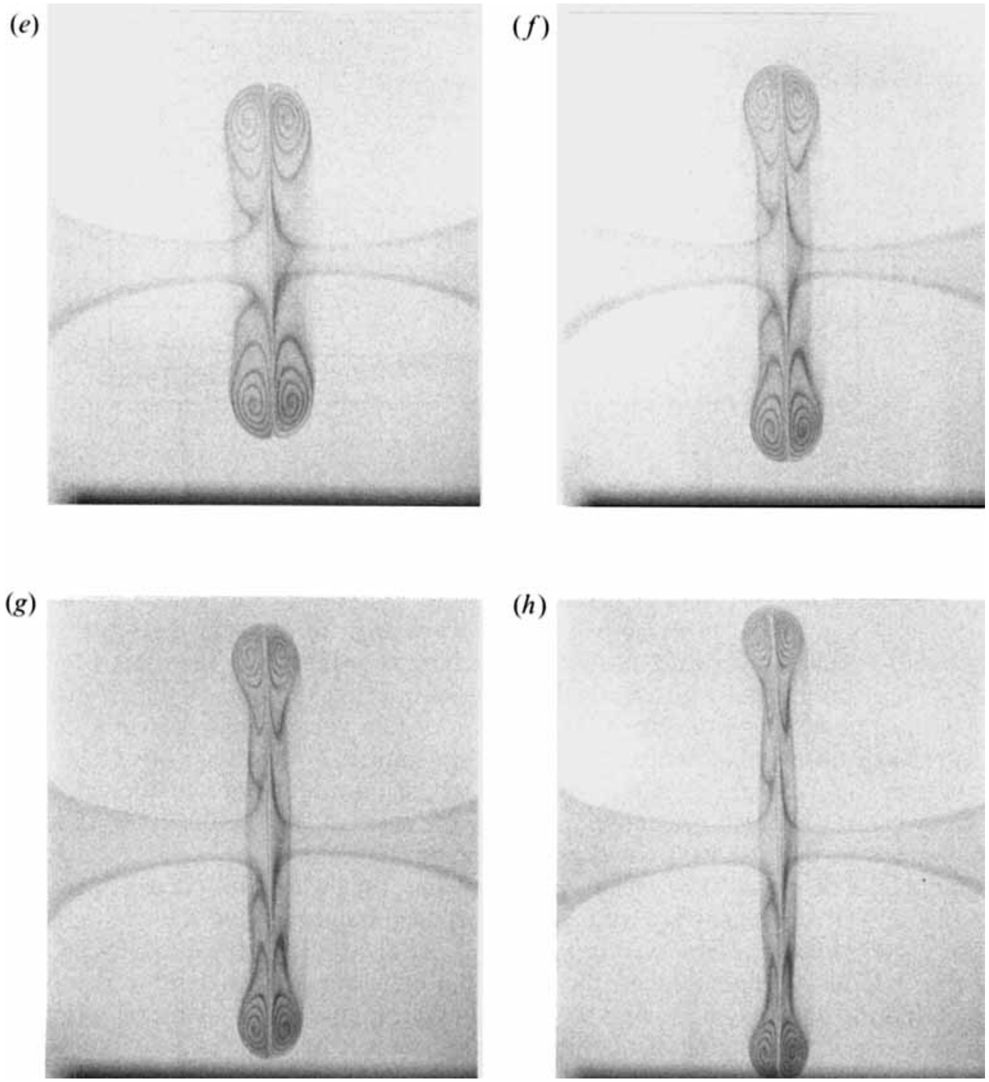

FIGURE 5. Results of flow visualization obtained by photochromic timelines at $Re_\Gamma \approx 1500$ with $c_0 \approx 0.18$ and $s_0 \approx 8$. (*a*) $t \approx 10.0$; (*b*) $t \approx 13.3$; (*c*) $t \approx 15.0$; (*d*) $t \approx 16.6$; (*e*) $t \approx 18.3$; (*f*) $t \approx 20.0$; (*g*) $t \approx 21.6$; (*h*) $t \approx 23.3$.

domain of $[0, W] \times [0, H] = [0, 20] \times [0, 14]$ in (r, z)-space is sufficient for the present calculations. The dependence of the calculated enstrophy on the grid point distribution will be presented in figure 11. The calculations were performed on a Cray-YMP-EL; each timestep took about 1 CPU s.

4.3. *Basic flow features*

The general flow features observed in the head-on collision of two coaxial vortex rings are presented as follows. Figure 5 displays a sequence of photographs, taken by a Nikon F3 camera with a motor drive, which present the evolution of the head-on collision of two vortex rings at $Re_\Gamma \approx 1500$ with $c_0 \approx 0.18$ and $s_0 \approx 8$. The photographs shown in figure 5 are the images of the meridian cross-section of the vortex rings marked by photochromic-dye tracers. Figure 5 shows that, when the two vortex rings

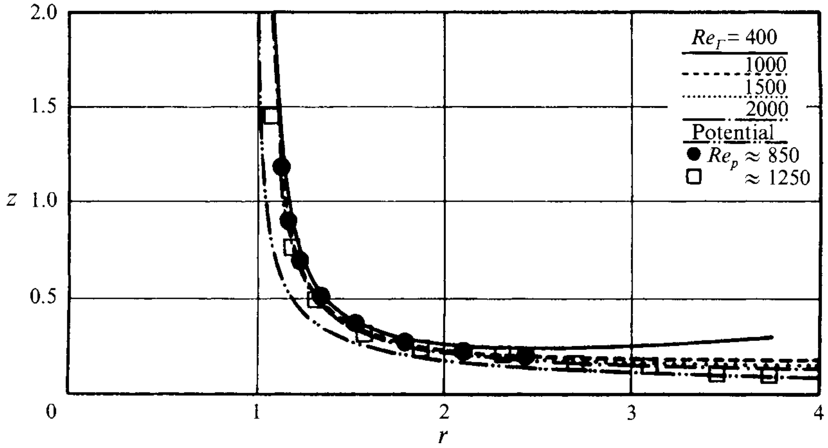

FIGURE 6. Trajectories of the loci of the vortex-ring core for various Reynolds numbers; vortex centres by flow visualization and vorticity centres by numerical calculation.

had opposite senses of rotation travelling towards each other, the velocity induced by one vortex ring on the other caused both vortex rings to grow in diameter and to proceed to stretch the vortex. During the stretching of vortex rings, the shape of a head with a long trailing tail was observed on meridian cross-sections as shown in figure 5(*f–h*). The plane of symmetry of the collision of two vortex rings drawn in figure 1 is also clearly observed in figures 5(*c–d*). The trajectories of the dyed vortex centre for $Re_\Gamma \approx 850$ and 1250 are shown in figure 6, where the trajectories of the calculated vorticity centres are also presented, including the cases of $Re_\Gamma = 400$, 1000, 1500 and 2000 as well as the case of inviscid calculation with a finite core.

The results of global flow visualization indicate that when the vortex rings came together and stretched actively with each other, dyed bulges around the circumference of the vortex rings were observed to appear (cf. Khorrami 1991; Lim & Nickels 1992) for $Re_\Gamma > 1500$. At this moment, the azimuthal component of velocity must exist in bulges and the flow may no longer be axisymmetric. Figure 7 shows an example of the oblique view of the bulging instability at various values of time for $Re_\Gamma \approx 2100$ with $c_0 \approx 0.14$ and $s_0 \approx 8$. It is seen in figure 7 that several dyed bulges were observed to develop around the circumference of the vortex rings when their radii had increased to about four times the initial radius (i.e. $r_v = R_v^*/R_0^* \approx 4$); however, the dyed bulges continued to grow and then distorted instead of breaking-up towards the end of collision. It was found that the onset of bulging instability depended on the Reynolds number, Re_Γ, the initial separation of two vortex rings, s_0, and the core-size, c_0, of the vortex ring. Figure 8(*a*) presents the onset boundary of bulging instability in the Re_Γ *vs.* c_0 diagram obtained by collecting the visual result of all different D/L by varying initial separation of vortex rings, s_0. The onset boundary of bulging instability associated with various initial separations, s_0, are marked as narrow regions instead of single lines in order to include the uncertainty of the laboratory observation. It is noticed that the visualized results were obtained along the three D/L curves; therefore, the onset region associated with each s_0 was connected based on the three sets of visualized data. It is assumed that the regions between the three D/L curves follow a trend similar to those observed along the three D/L curves. Figure 8(*a*) shows that, apparently, the Reynolds number associated with the onset of bulging instability increases with the increase of the initial separation of two vortex rings, s_0, while under

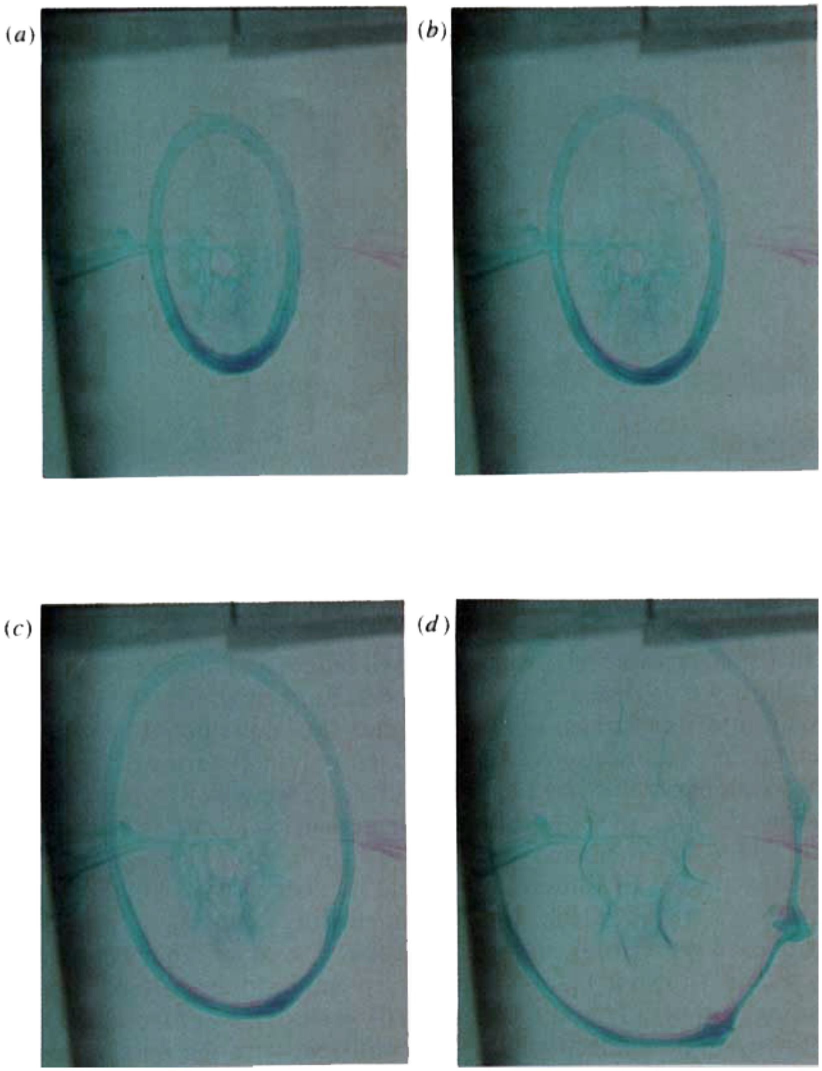

FIGURE 7. (*a*) An oblique view showing the bulging instability during collision for $Re_\Gamma \approx 2100$ with $c_0 = 0.14$, at $t = 21$, 23.2, 2.32 and 45.2, respectively.

the same initial separation, s_0, the bulging instability will be observed, basically, at a higher Re_Γ for a vortex ring with a smaller core-size, c_0, in the range of observation. For a specified onset boundary, the bulging instability will be observed to appear if the initial condition of two vortex rings, including Re_Γ, c_0 and s_0, locates on the left-hand side of this boundary. For example, the case of $Re_\Gamma = 1800$ with $c_0 = 0.12$ will be a stable case or a case without bulging instability as long as the initial separation of the two vortex rings, s_0, is larger than 8 while the case of $Re_\Gamma = 1800$ with $c_0 = 0.15$ will be an unstable case if $s_0 \leqslant 6$. Visual results also indicate that the smaller the core-size of a vortex ring is, the smaller the value of r_v associated with the onset of the bulging instability will be. On average, the values of r_v associated with the first appearance of dyed bulges were about 3.2, 4 and 5.4 for $D/L = 2.6$, 2.1 and 1.6, respectively. In figure 8(*a*), we also observe that, for an onset boundary associated with a fixed s_0, once Re_Γ reaches the critical value for bulging instability, the increase of Re_Γ

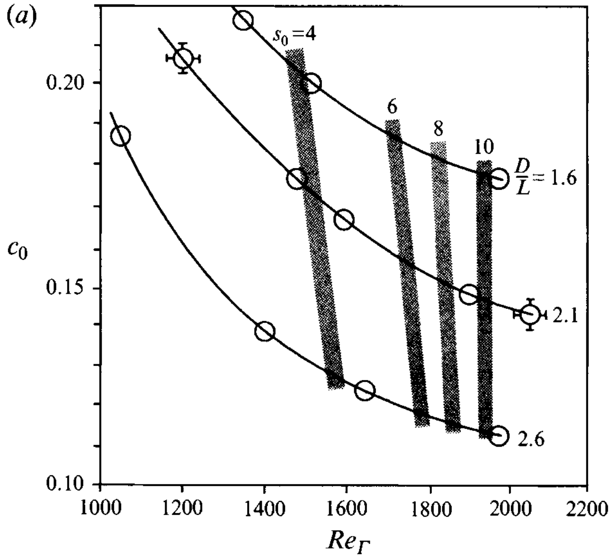

FIGURE 8 (*a*). For caption see facing page.

will result in a smaller value of r_v when the dyed bulges first appear. As Re_Γ continued to increase, short-waves were observed to appear. For higher Re_Γ, the bulges grew and then broke up into small rings. For even higher Re_Γ, flows could become turbulent. These observed flow features such as short waves and small vortex rings are consistent with the observations obtained by Lim & Nickels (1992). Figure 8(*b*) presents a sequence of photographs showing the observed flow phenomena when Re_Γ was increased along the curve of $D/L = 1.6$, indicated in figure 8(*a*), while the initial separation of vortex rings, s_0, was fixed to 8. In addition, the initial number of dyed bulges was eight (see figure 8(*b*), $Re_\Gamma \approx 1800$) which were symmetrically distributed around the circumference of each vortex ring, and increased as Re_Γ went up. The phenomenon in the case of $Re_\Gamma \approx 2700$ shown in figure 8(*b*) was very similar to the pattern observed in the aircraft trailing vortices. The number of small vortex rings observed in the case of $Re_\Gamma \approx 2700$ was about eighteen which was consistent with the observation made by Lim & Nickels (1992). They also estimated the wavelength of the instability according to Crow's inviscid model (Crow 1970) by counting the number of vortex rings and obtained a rough agreement with their experimental observations. Discussion will be continued in §4.5 for bulging instability.

On the other hand, the flow feature of rebound was observed to be associated with low-Reynolds-number cases shown in figure 6; that is, the calculated vorticity centres gradually moved toward each other and eventually moved away or rebounded from the plane of symmetry during collision. Because it is difficult to obtain perfectly symmetric images from flow visualization at low Reynolds numbers especially for $r_v > 3$ during vortex stretching, in the present study, the rebound phenomenon of the vorticity centre of a vortex ring is identified based on the results of numerical calculation. Although the results of Oshima (1978) and Kambe & Mya Oo (1984) might imply this feature, the rebound phenomenon was not addressed in their reports. The detailed mechanism of rebound phenomenon will be discussed in §4.6.

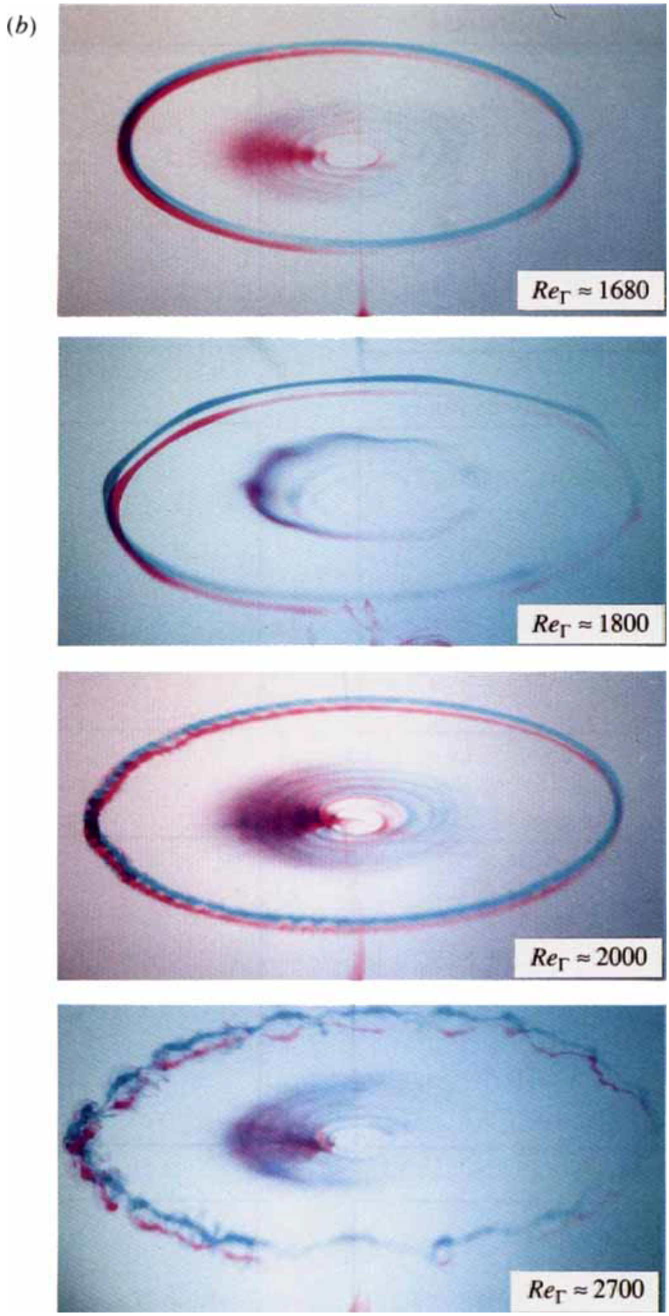

FIGURE 8. (*a*) The onset boundary of bulging instability in the Re_Γ to c_0 diagram obtained by collecting the visual results of all different orifice-diameter to piston-stroke ratio, D/L, under varying initial separation of vortex rings, s_0, where the onset boundaries of bulging instability are marked according to the various initial separation, s_0. Note that the open circles shown in the figure are the measured data points for c_0; typical error bars for Re_Γ and c_0 are also shown in the figure. (*b*) Photographs presenting the observed flow phenomena including no bulging instability, bulging instability, short waves and small vortex rings with increasing Re_Γ along the curve $D/L = 1.6$ shown in (*a*).

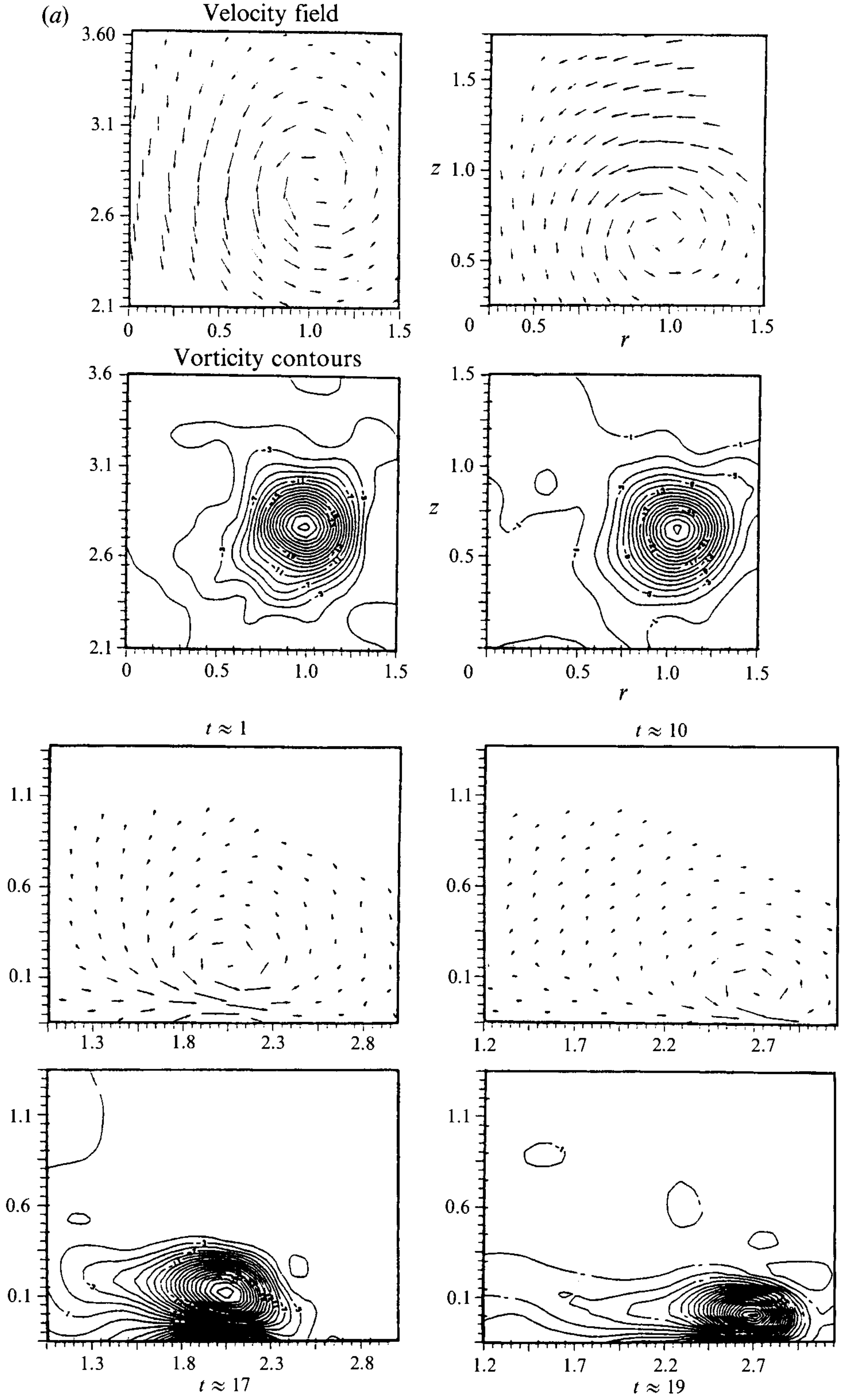

FIGURE 9 (*a*). For caption see facing page.

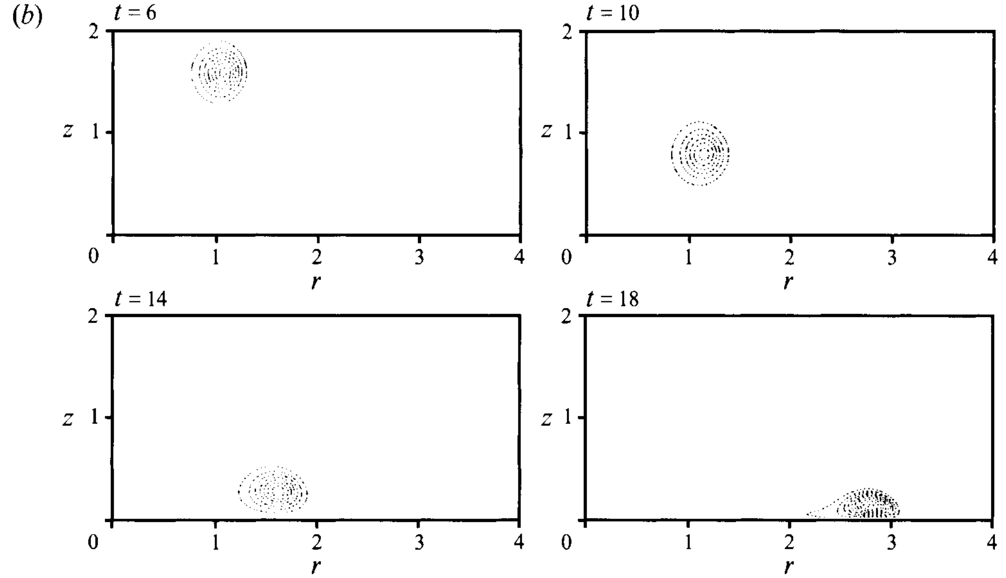

FIGURE 9. (*a*) Measured velocity field and vorticity distribution at different times for $Re_\Gamma \approx 2070$ with $c_0 = 0.14$ and $s_0 = 6$. (*b*) Vorticity contours at different times for $Re_\Gamma = 2000$ with $c_0 = 0.15$ and $s_0 = 6$ obtained by numerical simulation.

4.4. *Three stages of vortex evolution*

More flow physics, especially the vortex evolution associated with the head-on collision of two vortex rings, will be revealed based upon the present experimental and numerical results. Figure 9(*a*) presents an example of the results of the large-field measurement for $Re_\Gamma \approx 2070$ with $c_0 \approx 0.14$ and $s_0 = 6$, including the instantaneous velocity field and equivorticity lines at various times while figure 9(*b*) presents the equivorticity lines obtained from numerical simulation for $Re_\Gamma = 2000$ with $c_0 = 0.15$ and $s_0 = 6$ at different times. It is noticed that each set of the instantaneous velocity field and its corresponding equivorticity lines at various times shown in figure 9(*a*) were reconstructed from different runs of experiment under the criterion presented in §3.2.4. For each time instant, the velocity field and vorticity contours was obtained by a single experiment without any average involved. It shows good agreement between the calculated results and those shown in figure 9(*a*). The details of data reduction and the estimation of uncertainty were presented in Chu & Liao (1992). The uncertainty associated with the equivorticity contours was about 1.5/s which was about 4–6% of the measured peak vorticity. In addition, figure 10 shows good agreement between the calculated and the experimental results of the evolution of circulation and enstrophy for various Re_Γ. The time evolution of circulation, shown in figure 10, is qualitatively similar to the result obtained by Stanaway *et al.* (1988) though the initial vorticity distribution was different. Circulations associated with the vortex rings were obtained by integrating along the boundaries of the specified regions according to the vorticity distribution. The total enstrophy, E, $\frac{1}{2}\int_V \omega^2 \mathrm{d}V$, in any specified volume was also estimated by calculating the square of vorticity in the annulus. Thus, in figure 10, the maximum uncertainty in the estimation of the enstrophy will be around 10% which is approximately twice the value of the uncertainty of vorticity. Regarding the uncertainty of the circulation, it would be less than that of enstrophy due to the integration of $(\boldsymbol{u}\cdot\mathrm{d}\boldsymbol{l})$ was calculated instead. Recall that the values of the qualified data are within 5%

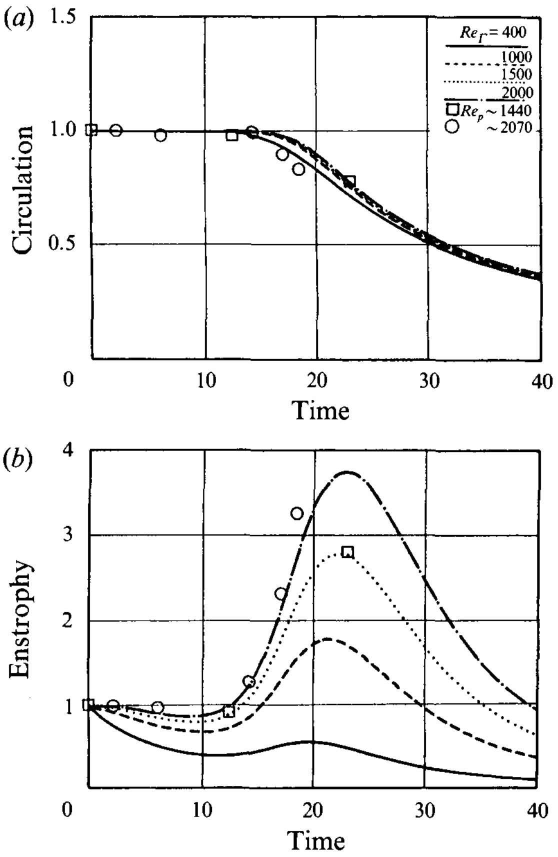

FIGURE 10. The time evolution of (*a*) circulation and (*b*) enstrophy for various Reynolds numbers – experimental and numerical results. Note that the values of enstrophy have been normalized by their initial values.

variation of the mean value before the vortex rings interact with each other. However, this amount of variation would increase with increasing vortex ring diameter owing to the limit of the spatial resolution in the present measurement technique. When the amount of variation was over 10 % of the mean value we stopped sampling the data thereafter. The trend of changes of circulation and enstrophy in the present study are similar to those of the numerical simulation by Kambe & Mya Oo (1984).

To gain further insight into the vortex evolution, first, the fundamental equations will be used to analyse the variations of circulation and enstrophy of the vortex rings during the evolution of head-on collision. Then, the results will be discussed based upon these analyses.

Consider the loop 1–2–3–4–1 denoted by C in figure 1. The circulation Γ, is defined to be $\oint_C \boldsymbol{u}\cdot \mathrm{d}\boldsymbol{l}$, and its rate of change can be written as

$$\frac{\mathrm{d}\Gamma}{\mathrm{d}t} = -\frac{1}{Re_\Gamma}\oint_C (\nabla \times \boldsymbol{\omega})\cdot \mathrm{d}\boldsymbol{l} = -\frac{1}{Re_\Gamma}\oint_C \left[-\frac{\partial \omega}{\partial z}\mathrm{d}r + \left(\frac{\omega}{r}+\frac{\partial \omega}{\partial r}\right)\mathrm{d}z\right], \tag{4.1}$$

where we recall that ω is the azimuthal component of vorticity normal to the (r, z)-plane. It should be noted that the contour C, 1–2–3–4–1, is large enough to include all vorticity concerned.

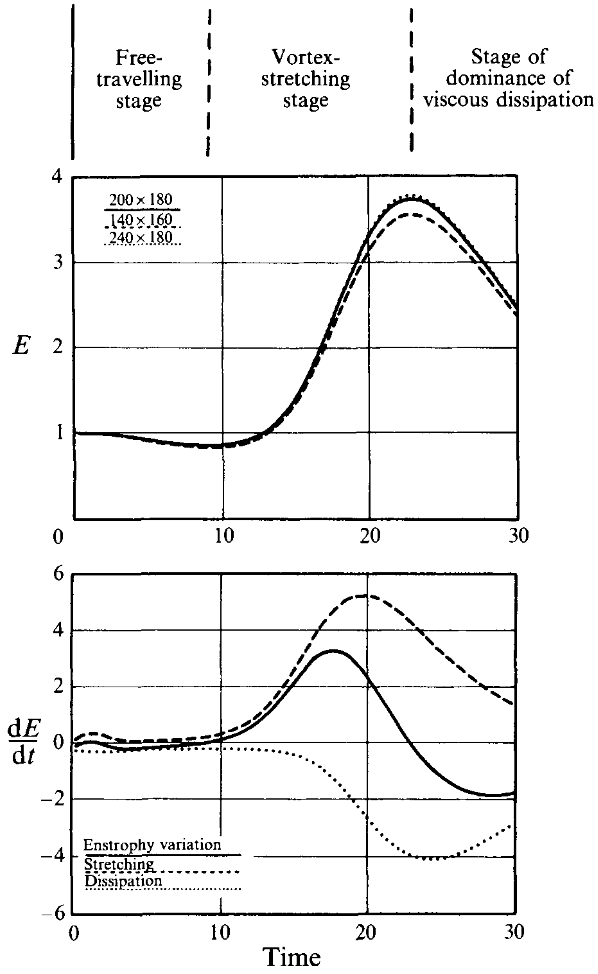

FIGURE 11. (*a*) The dependence of the evolution of enstrophy on the grid point distribution for $Re_r = 2000$; (*b*) the variation of enstrophy according to (4.2) for $Re_r = 2000$, including the effect of vortex stretching and that of viscous dissipation.

Let V be the volume specified as the revolution about the z-axis of the area S surrounded by 1–2–3–4–1 according to figure 1. The total enstrophy E, $\frac{1}{2}\int_V \omega^2 \,\mathrm{d}V$, is always positive and can be considered to be a quantitative measure of the vortical activity of a vortex motion. The rate of change of the total enstrophy in cylindrical coordinates can be expressed as

$$\frac{\mathrm{d}E}{\mathrm{d}t} = \int_S \left[2\pi\omega^2 u_r - \frac{1}{Re} 2\pi r \left[\left(\frac{\partial \omega}{\partial z}\right)^2 + \left(\frac{\omega}{r}\right)^2 + \left(\frac{\partial \omega}{\partial r}\right)^2 \right] \right] \mathrm{d}r\,\mathrm{d}z. \tag{4.2}$$

The first term in the integrand of (4.2) represents the effect of vortex stretching, which typically will enhance the total enstrophy during vortex stretching while the second term is a sink term to $\mathrm{d}E/\mathrm{d}t$, signifying the effect of viscous dissipation. Figure 11 shows a typical example of the variation of enstrophy by numerical calculation according to (4.2) for $Re_r = 2000$ with $c_0 = 0.15$ and $s_0 = 6$. Apparently, the time rate of change of the total enstrophy depends on the competition between vortex stretching and viscous dissipation, and each of them is dominant at different stages during the collision. Compare the two plots shown in figure 11. It is meaningful to separate the whole evolution of the head-on collision of two coaxial vortex rings or of a vortex ring approaching a stress-free surface into three stages, i.e. the free-travelling stage, vortex-stretching stage, and stage of dominance of viscous dissipation. These are similar to those mentioned by Chu *et al.* (1993) in their study of a vortex ring normally approaching a solid surface or a slightly contaminated free surface, in which the whole evolution can be separated into three stages, i.e. the free-travelling stage, vortex-stretching stage, and vortex-rebounding stage. Figure 11 also presents the dependence of the numerical calculation on the grid distribution. Recall that 200 × 180 grid points distributed in (r, z)-space were used in the present study for $Re_\Gamma = 2000$.

In this vortex-ring flow, the relationship between the rate of change of total kinetic energy, K, and the enstrophy can be represented by the following equation:

$$\frac{\mathrm{d}K}{\mathrm{d}t} = -\frac{2}{Re_\Gamma}\int_V \tfrac{1}{2}\omega^2\,\mathrm{d}V = -\frac{2}{Re_\Gamma}E. \tag{4.3}$$

In the present study, vortex rings are completely formed at about 2.5 times the orifice diameters downstream of the exit of the orifice. In addition, no azimuthal instability is observed in vortex rings just when the collision of the vortex rings begins. Therefore, the experimental conditions match the assumptions of the above analyses. In the following, we will focus on the variations of circulation, enstrophy, and kinetic energy of the vortex ring during the three stages of head-on collision prior to the appearance of azimuthal instability.

4.4.1. *Free-travelling stage*

When a vortex ring is in the free travelling stage, it is the viscous diffusion that causes the decrease of peak vorticity in the vortex ring centre. The experimental evidence (see figure 9) confirms this observation.

In the free-travelling stage, suppose the integration loop 1–2–3–4–1 shown in figure 1 is considered, and the vorticity gradient is zero when r is large; thus, (4.1) can be further reduced to

$$\frac{\mathrm{d}\Gamma}{\mathrm{d}t} = -\frac{2}{Re_\Gamma}\int_\infty^0 \left.\frac{\partial\omega}{\partial r}\right|_{r=0}\mathrm{d}z. \tag{4.4}$$

Figures 9(a, b) show that the vorticity gradients are small near the z-axis of the vortex ring; thereafter, a slight change of circulation is expected when the vortex rings are some distance apart. Figure 10(a) shows that the trend of the variation of circulation agrees with the analysis.

As far as the change of enstrophy is concerned, the first term on the right-hand side of (4.2) is negligible because of the lack of significant stretching and owing to the small vorticity gradient as well as the magnitude of vorticity. Thus, (4.2) can be further simplified as

$$\frac{\mathrm{d}E}{\mathrm{d}t} = -\frac{1}{Re_\Gamma}\int_S 2\pi r\left[\left(\frac{\partial\omega}{\partial z}\right)^2 + \left(\frac{\omega}{r}\right)^2 + \left(\frac{\partial\omega}{\partial r}\right)^2\right]\mathrm{d}r\,\mathrm{d}z. \tag{4.5}$$

Definitely, the enstrophy will decay when the vortex ring is in the free-travelling stage according to (4.5). The variations of enstrophy shown in figure 10(b) indicate a similar trend of dependence on the Reynolds number. The present results also show agreement with the previous study by Chu *et al.* (1993).

4.4.2. *Vortex stretching stage*

When the vortex rings come close enough, they interact with each other and proceed to vortex stretching. The results of flow visualization show that, during head-on collision, the vortex ring will increase in size to about four times its initial diameter. The severe stretching causes a sudden increase of peak vorticity. This can be seen in the vorticity contours of figure 9.

Figure 10(*a*) shows that the circulation of a vortex ring decays gradually during vortex stretching. As we follow the loop 1–2–3–4–1 shown in figure 1, (4.1) can be reduced to

$$\frac{\mathrm{d}\Gamma}{\mathrm{d}t}=\frac{1}{Re_\Gamma}\int_0^\infty \left.\frac{\partial\omega}{\partial z}\right|_{z=0}\mathrm{d}r-\frac{2}{Re_\Gamma}\int_\infty^0 \left.\frac{\partial\omega}{\partial r}\right|_{r=0}\mathrm{d}z. \tag{4.6}$$

The results shown in figures 9(*a, b*) indicate that both terms on the right-hand side of (4.6) are negative in sign; the value of the circulation Γ of 1–2–3–4–1 will therefore decrease as time is increasing. The results shown in figure 10(*a*) agree with this analysis.

It is shown in (4.2), apparently, that the variation of enstrophy depends on the competition between vortex stretching and viscous dissipation. Figure 10(*b*) shows that the enstrophy has a sudden increase in the early stage of vortex stretching because of the dominance of the stretching effect, represented by the first term inside the integrand of (4.2). Until the scale of the vortex ring core decreases to a certain limit owing to stretching, the vorticity gradients become so large that the contribution of the viscous dissipation term in (4.2) overcomes that of the stretching term (see figure 11). Therefore, the enstrophy will decrease again as shown in figure 10(*b*). On the other hand, the sudden increase of the enstrophy during the stretching process will enhance the dissipation of the total kinetic energy of the vortex ring according to (4.3). Thus, during vortex stretching, the enhancement of the vortical activity is always accompanied by a speeding up of energy dissipation.

4.4.3. *The stage of dominance of viscous dissipation*

As shown in figures 10(*b*) and 11, when enstrophy reaches its peak value, the vortex evolution shifts to the stage of dominance of viscous dissipation. From that moment on, the effect of viscous dissipation overcomes that of vortex stretching. However, results from flow visualization and numerical calculation indicate that flow features associated with the stage of dominance of viscous dissipation, rebound or bulging instability, depend on the Reynolds number and the initial separation between vortex rings. Now, we present the details of bulging instability and rebound in the following sections.

4.5. *Bulging instability*

As shown in figure 8(*a*), the phenomenon of bulging instability depends primarily on the Reynolds number, Re_Γ, the initial separation of vortex rings, s_0, and the core-size of the vortex ring, c_0. In addition, the radii of vortex rings associated with the appearance of dyed bulges were about three, four and five times their initial values for the orifice-diameter to piston-stroke ratio, $D/L = 2.6$, 2.1 and 1.6, respectively. Further discussion will be focused on the quantitative aspect of the onset of bulging instability via numerical computation such that a local dimensionless group would be expected, which may characterize the onset for bulging instability around the circumference of vortex rings during collision.

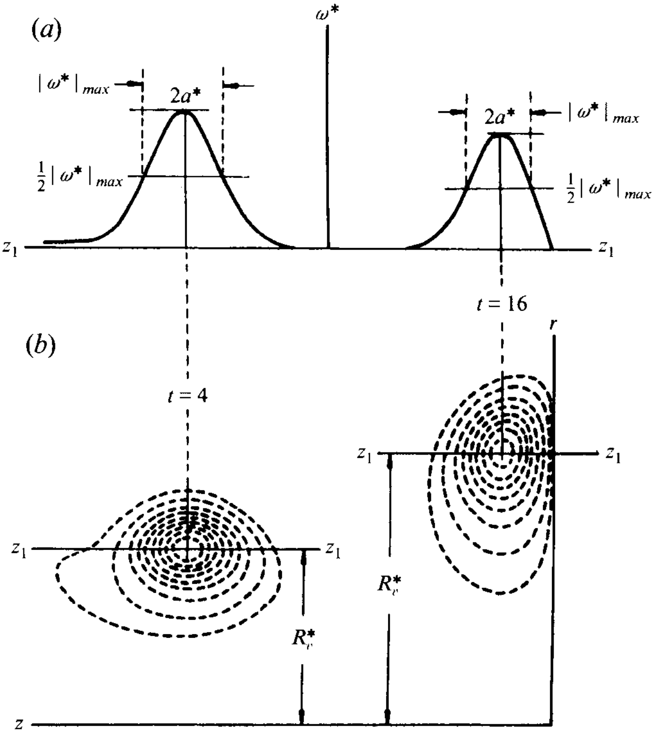

FIGURE 12. (*a*) An example of vorticity distribution along the (z_1, z_1)-axis for $Re_\Gamma = 1000$ with $c_0 = 0.20$ and the definition of the diameter of the vorticity core $2a^*$; (*b*) the radius of a vortex ring at various times, where the contours are the equivorticity lines.

A qualified candidate of the dimensionless group should be responsible for both global and local evolutions during vortex stretching. Let us consider the situation associated with the vortex ring during collision. The vortex lines of a vortex ring are subjected to stretching in its azimuthal direction. The instant peak of vorticity at the vorticity centre, $|\omega^*|_{max} = |\omega^*|_{max}(t)$, and the diameter of the vorticity core, $2a^* = 2a^*(t)$, defined as the distance in the z-direction between the locations where the value of local vorticity decreases to $\frac{1}{2}|\omega^*|_{max}$ as shown in figure 12(*a*) according to the vorticity distribution along the (z_1, z_1)-axis, are the key parameters in response to the local evolution of a vortex ring. As far as global evolution is concerned, the radius of a vortex ring, $R_v^* = R_v^*(t)$, or the radius of curvature of the vortex line passing through the vorticity centre adequately describes the increase in size of the vortex ring during collision. Accordingly, an instant dimensionless parameter, N_t, which is defined by $N_t = (2a^*|\omega^*|_{max} R_v^*)/\nu = 2a|\omega|_{max} r_v Re_\Gamma$ or $N_t/Re_\Gamma = 2a|\omega|_{max} r_v$, may characterize the onset for bulging instability along the circumference of a vortex ring, where $a = a^*/R_0^*$, $|\omega|_{max} = |\omega^*|_{max}(R_0^{*2}/\Gamma_0^*)$ and $r_v = R_v^*/R_0^*$. We think that the bulging instability is not merely a lengthscale or a velocity-scale problem. The definition of N_t incorporates the (global) lengthscale as well as (local) velocity scale implicitly. This dimensionless number is different from the local Rossby number defined by Spall, Gatski & Grosch (1987), which deals with the vortex breakdown in vortices with a strong axial velocity such as trailing wing-tip and leading-edge vortices. In the following, the evolution of N_t/Re_Γ will be presented, since, as indicated, N_t itself involves the Reynolds number effect. Recall that for the same Re_Γ, the core-size, c_0, of a vortex ring will be different owing to the difference of D/L, and thus the value of N_t/Re_Γ will be a function of c_0 implicitly.

Refer to figure 8(*a*); the cases with core-size $c_0 = 0.15$ can be chosen as typical examples to examine the evolution of N_t/Re_Γ since it crosses several onset boundaries of bulging instability as Re_Γ increases. Figure 13(*a*) presents the evolution of N_t/Re_Γ during collision for the core-size $c_0 = 0.15$, which includes the results of $Re_\Gamma = 1500$, 1800 and 2000. For each Re_Γ shown in figure 13(*a*), the initial separation of $s_0 = 4$, 6 and 8 was studied, respectively. Let us first examine the result of $Re_\Gamma = 1800$ with $c_0 = 0.15$. It is seen in figure 8(*a*) that the onset of bulging instability should occur between $s_0 = 6$ and 8, which is about 7. By examining the evolution of N_t/Re_Γ presented in figure 13(*a*), it appears that there exists a threshold $(N_t/Re_\Gamma)_{cr}$ or a sufficient condition of N_t/Re_Γ for bulging instability, which is about 6.3, and that over this bulging instability will occur. Let us further examine the case of $Re_\Gamma = 2000$ with $c_0 = 0.15$. The calculated result shown in figure 13(*a*) indicates that the values of N_t/Re_Γ exceed the threshold or 6.3 for both $s_0 = 6$ and 8 during collision. Therefore, the appearance of bulging instability is guaranteed. With regard to the case of $Re_\Gamma = 1500$ with $c_0 = 0.15$, according to figure 13(*a*), the maximum value of N_t/Re_Γ is very close to, but less than, the critical value, 6.3 for the initial separation of $s_0 = 4$. Therefore, the case of initial separation $s_0 = 4$ is a marginal case in the sense of the onset of bulging instability, not to mention $s_0 = 6$ and 8. The experimental observation shown in figure 8(*a*) does confirm these judgements. In addition, figure 13(*b*) presents the time evolution of the calculated radius of vortex ring during collision for the cases of $c_0 = 0.15$. Figure 13(*b*) shows that, for the case of $Re_\Gamma = 1800$ with $s_0 = 7.2$ which is very close to the onset boundary, the radius is about four when the peak value of N_t/Re_Γ occurs as indicted in figure 13(*a*), which is consistent with the result observed in flow visualization. Furthermore, for the case of $Re_\Gamma = 2000$ with $s_0 = 8$, the radius is about 3.5 when the value of N_t/Re_Γ crosses the threshold, which also agrees with the result of flow visualization. The consistency of the radius-to-time relation further ensures the validity of the threshold for bulging instability.

Similarly, by combining the visual result shown in figure 8(*a*) and the result of calculation shown in figure 13(*c*), the threshold of N_t/Re_Γ for the core-size $c_0 = 0.12$ can also be found, which is about 6.8. For the case of $Re_\Gamma = 1800$ with $s_0 = 6$, the corresponding value of r_v shown in figure 13(*d*) is about 3.3 when N_t/Re_Γ crosses the critical value, which is very close to the result of flow visualization. Following the same procedure, the critical value of N_t/Re_Γ for the core-size $c_0 = 0.20$ can also be found, which is about 5.6. Therefore, vortex rings with a smaller core-size, c_0, will result in a higher critical value of N_t/Re_Γ for bulging instability.

Several salient features of the sufficient condition, N_t/Re_Γ, for bulging instability are described as follows. First, since ω_{max} is a function of time, $N_t/Re_\Gamma = 2a|\omega|_{max}\, r_v$ involves viscosity implicitly, though viscosity does not appear explicitly in this ratio. Secondly, for a vortex ring with a vorticity core diameter $2a$, the value of N_t/Re_Γ will be a function of r_v/a, for $|\omega|_{max} \sim \Gamma_0/a^2$ and $N_t/Re_\Gamma \sim 2a\Gamma_0 r_v/a^2 \sim r_v/a$. Figure 13(*a*, *c*) shows that vortex rings initially having a smaller c_0 or a larger r_v/a will result in a larger value of N_t/Re_Γ. Moreover, in the vortex stretching stage, the value of N_t/Re_Γ almost always increases linearly with the decrease of $2a/r_v$ for $2a/r_v > 0.075$ as indicated in figure 13(*e*). Thirdly, bulging instability of a vortex ring is typically observed in the stage of vortex stretching. This is in contrast to the cases for a single vortex ring observed by Maxworthy (1972) and Widnall, Bliss & Tsai (1974), which indicated that wavy instability would be observed instead of bulging instability. Figure 13(*a*, *c*) confirms that, during the free-travelling stage, the value of N_t/Re_Γ may even

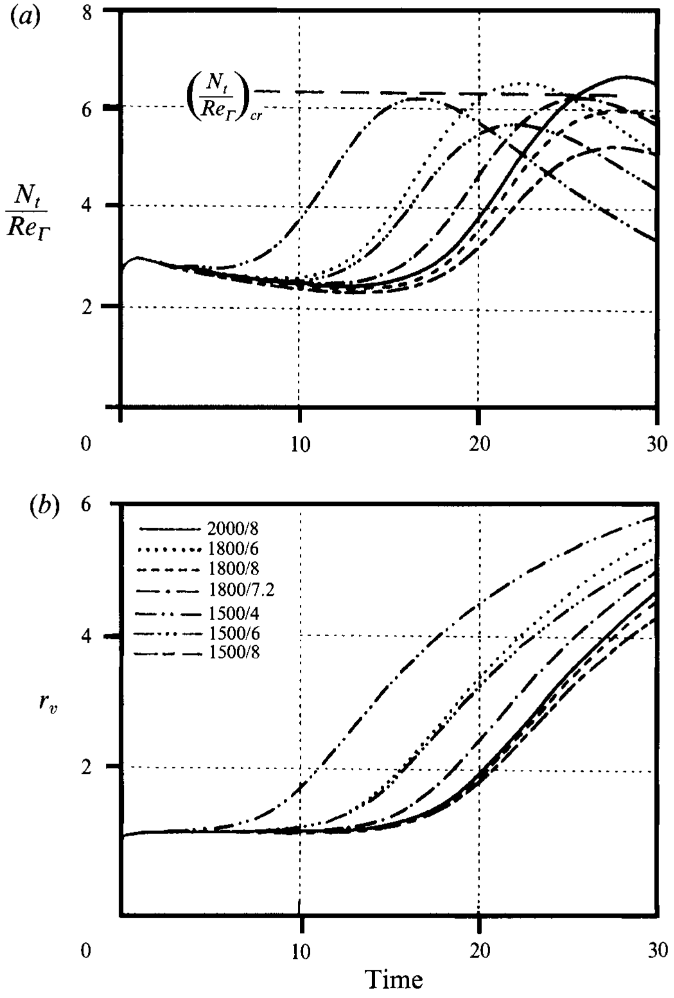

FIGURE 13 (*a*, *b*). For caption see p. 65.

decrease with the decrease of $r_v/2a$ owing to viscous diffusion. Lastly, the value of N_t/Re_Γ is not a ratio of circulation according to the definition of N_t; otherwise, the value of N_t/Re_Γ definitely would decrease during collision because of the decrease of circulation in the vortex stretching stage shown in figure 10(*a*).

On the other hand, an interesting necessary condition related to bulging instability was also observed based on the present calculation, which is the evolution of $2a/r_v$, the vorticity core diameter to vortex ring radius ratio, presented in figure 13(*f*). It is found that when bulging instability occurs, the value of $2a/r_v$ is always about 0.06. Nevertheless, for all of the cases shown in figure 13(*a*, *c*), though the values of $2a/r_v$ decrease to 0.06 during collision, bulging instability does not necessarily occur, depending on whether the sufficient condition, N_t/Re_Γ, is met or not. In addition, the observation of $2a/r_v \approx 0.06$ associated with the appearance of bulging instability provides strong evidence that vortex rings having a smaller core-size, c_0, or a smaller initial value of $2a/r_v$ will result in a smaller radius, r_v, when the onset of bulging instability appears while vortex rings having a larger initial value of c_0 or $2a/r_v$ will need farther stretching to satisfy $2a/r_v \approx 0.06$. This is consistent with the result

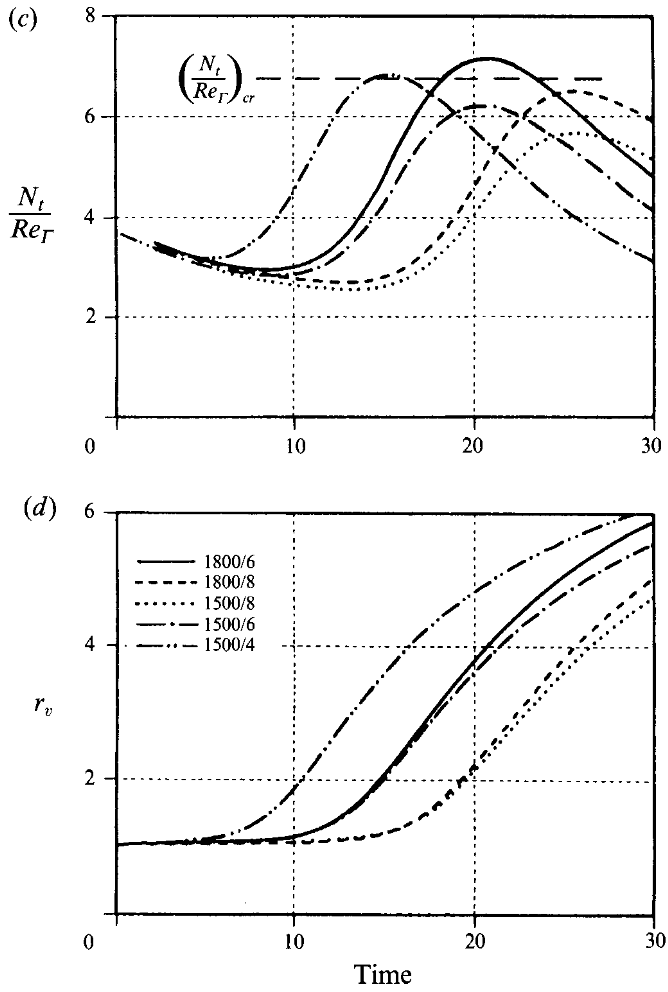

FIGURE 13 (*c*, *d*). For caption see p. 65.

observed in flow visualization as addressed in §4.3. Recall that the radii of vortex rings associated with the onset of bulging instability were about three, four and five times their initial values for the orifice diameter to stroke ratio, $D/L = 2.6$, 2.1 and 1.6, respectively.

4.6. *Rebound phenomena*

As indicated in figure 6, for lower Re_Γ, the calculated vorticity centres gradually moved towards each other and eventually moved away or rebounded from the plane of symmetry during collision. Actually, some of the cases shown in figure 13(*a*, *c*) which do not meet the sufficient condition of bulging instability will, however, also lead to the rebound phenomenon according to the level-off in the $2a/r_v$ *vs*. time relation presented in figure 13(*f*); that is, the vorticity core diameter, $2a$, decreases during the stage of vortex stretching and then increases again with the increase of the vortex ring radius, r_v, during the stage of dominance of viscous dissipation. Thus, the vorticity centre retreats or rebounds from the plane of symmetry. This rebound is different from the rebound observed in a vortex ring impinging normally on a solid plane surface, which is due to the formation of a secondary vortex generated at the wall and the mutual

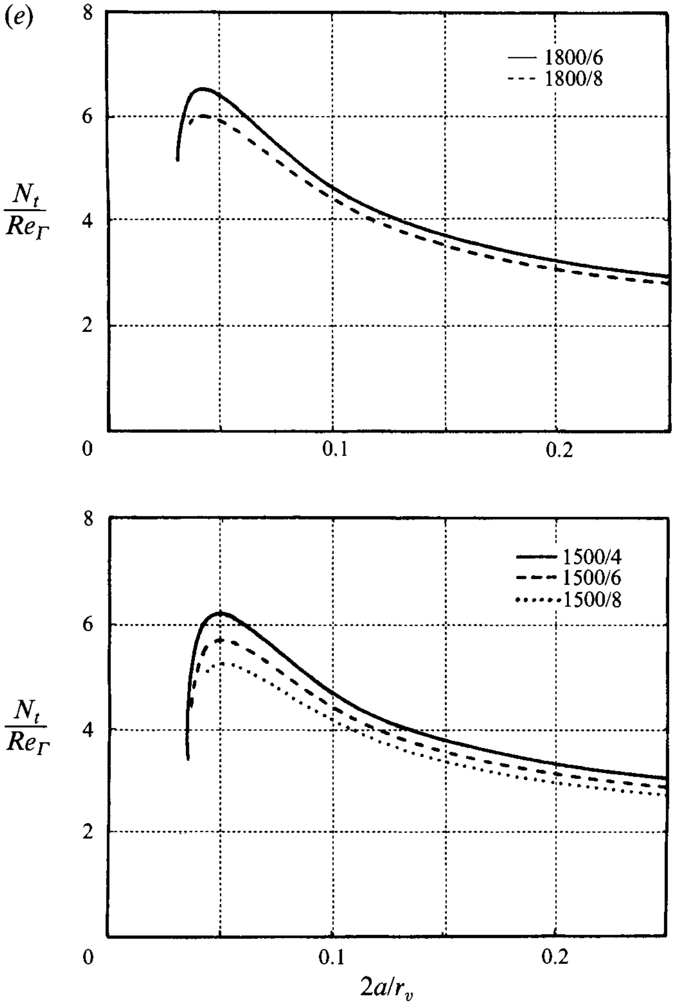

FIGURE 13 (*e*). For caption see facing page.

interaction between the primary and secondary ones. The present case, however, does not have new vorticity generated at the colliding surface. Therefore, what causes the rebound in the head-on collision needs to be further clarified. It is shown in figure 6 that this rebound phenomenon is more evident when Re_Γ is low. Thus, we focus on the cases of $Re_\Gamma < 1500$ for detailed discussion.

One may wonder about the difference between a vorticity centre and a visualized vortex centre. We show in figure 14(*a*) various trajectories of the flow field with $Re_\Gamma = 400$ and 1000, which includes the path traced out as time increases by the vorticity centre, *p.v.*, the particle path for that particle of fluid which was initially coincident with the vorticity centre at the initial instant $t = 0$, *p.t.*, and the path of the point at which the Stokes streamfunction has a local extremum (or a streamline centre), *p.s.* Figure 14(*b*) shows a close-up of the time evolution of *p.v.* in the z direction for $Re_\Gamma = 400$, 1000 and 1500, respectively. Of particular interest is the fact that the centre's rebound from the plane of symmetry, which occurs at $t \approx 23$ and 26 for $Re_\Gamma = 400$ and 1000, respectively, is indicated in all three trajectories. Peace & Riley

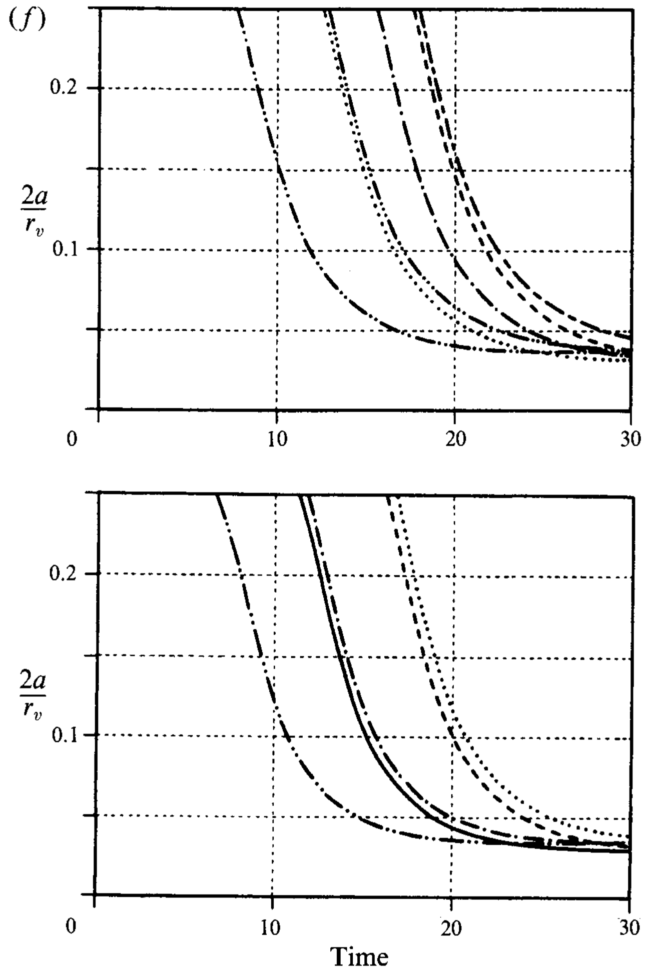

FIGURE 13. (*a*) Time evolution of N_t/Re_Γ for the cases of $c_0 = 0.15$; refer to (*b*) for the description of symbols; (*b*) time evolution of the dimensionless radius of the vortex ring during collision corresponding to (*a*), the calculated result, where the numbers, 1800/8 for example, means $Re_\Gamma = 1800$ and $s_0 = 8$; (*c*) time evolution of N_t/Re_Γ for the cases of $c_0 = 0.12$; refer to (*d*) for description of symbols; (*d*) time evolution of the dimensionless radius of the vortex ring during collision corresponding to (*c*), the calculated result, where the numbers, 1800/6 for example, means $Re_\Gamma = 1800$ and $s_0 = 6$; (*e*) relation between N_t/Re_Γ and $2a/r_v$ for $c_0 = 0.15$; and (*f*) time evolution of $2a/r_v$ for $c_0 = 0.15$ and 0.12, respectively; refer to (*b*) and (*d*), respectively, for description of symbols.

(1983) have reported on this phenomenon in a numerical simulation of a two-dimensional vortex pair approaching a zero-stress boundary. Peace & Riley attributed the rebound of a vortex pair to the sink of vorticity at the stress-free boundary and concluded that the rebound behaviour is essentially a viscous phenomenon. In the present study, the feature of vortex stretching has to be incorporated. Peace & Riley's explanation of the rebound in the absence of vortex stretching may not be sufficient in the present case. As shown in (4.6), the cancellation of circulation can only be examined along the boundaries; the major portion of the cancellation is along the colliding surface owing to the large gradients of vorticity in the z-direction along the

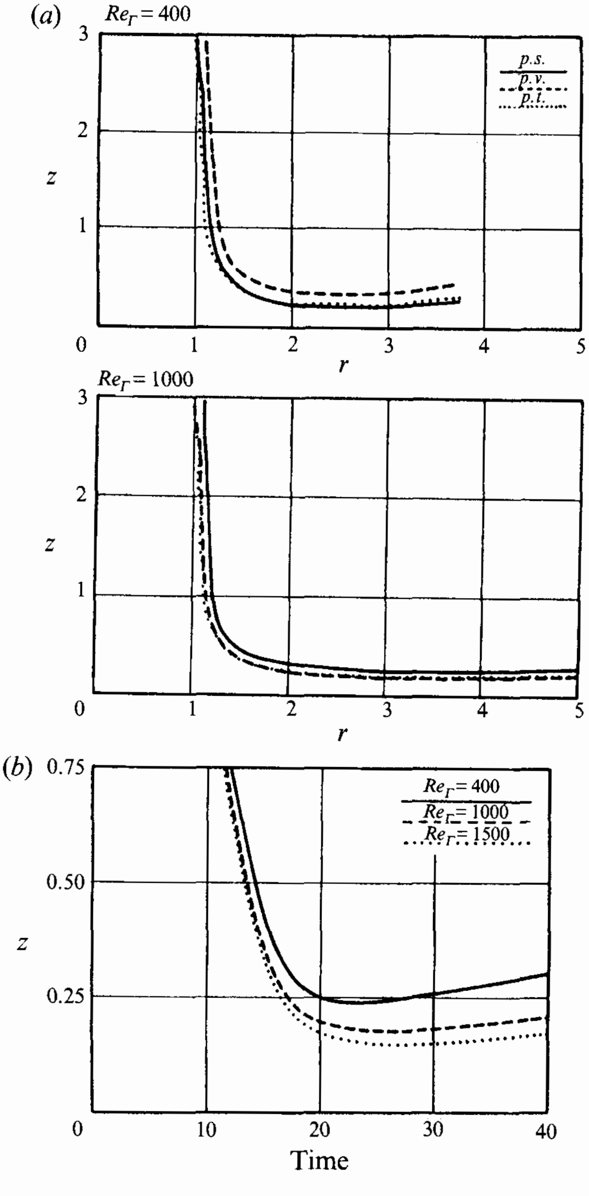

FIGURE 14. (*a*) Trajectories in the flow field for $Re_\Gamma = 400$ and 1000, where *p.v.* is the vorticity centre; *p.t.* is the particle trace initially coincident with the vorticity centre; and *p.s.* is the streamline centre. (*b*) A close-up of the time evolution of *p.v.* in the z-direction for $Re_\Gamma = 400$, 1000 and 1500 with $c_0 = 0.20$ and $s_0 = 6$.

colliding plane. The degradation of circulation is the decay of total vorticity mentioned by Peace & Riley (1983). However, in (4.2), the time variation of the total enstrophy, $\mathrm{d}E/\mathrm{d}t$, explicitly involves the effect of vortex stretching and viscous dissipation; their relative importance has to be assessed regarding the rebound phenomenon.

The case of $Re_\Gamma = 400$ with $c_0 = 0.20$ was used as an example for further detail in the variation of enstrophy. Figure 15(*a*) presents the evolution of $\mathrm{d}E/\mathrm{d}t$ and the respective effect due to the vortex stretching and viscous dissipation. Apparently, the magnitude of $\mathrm{d}E/\mathrm{d}t$ depends on the competition between vortex stretching and viscous dissipation

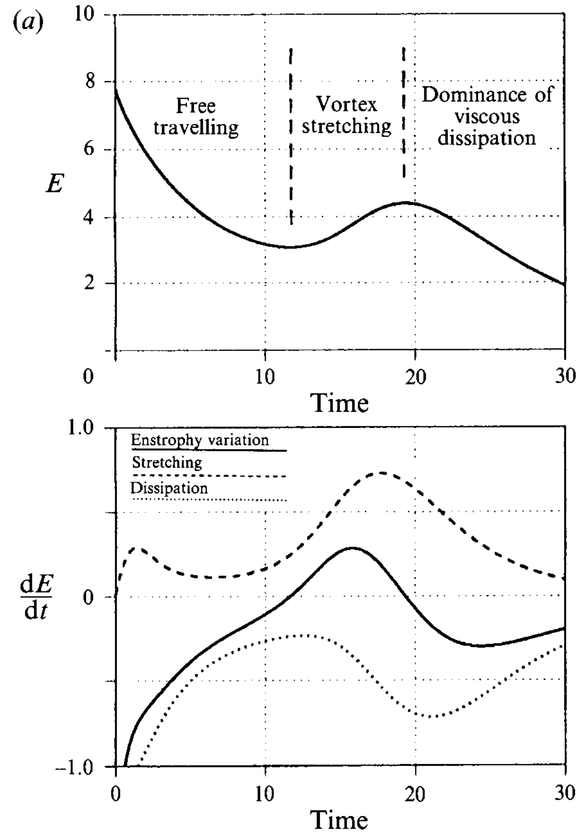

FIGURE 15 (*a*). For caption see p. 69.

as shown in the integrand of the right-hand side of (4.2). Regarding the distribution of the integrand of the right-hand side of (4.2), figure 15(*b*) presents the details. The contours of equivorticity for various values of time are also presented in figure 15(*c*) for reference. The lines in figure 15(*b*) plot magnitudes for the integrand of the right-hand side of (4.2) at various values of time, where the solid lines represent the contours of equimagnitude having positive contribution to the overall value of $\mathrm{d}E/\mathrm{d}t$ whereas the dotted lines represent the contours of equimagnitude with negative contribution to the overall value of $\mathrm{d}E/\mathrm{d}t$. Again, these lines show the net contribution incorporating the vortex stretching and the viscous dissipation. It is seen in figure 15(*b*) that, during the free-travelling stage, i.e. $t = 4$ or 10 for example, the region of positive contribution to $\mathrm{d}E/\mathrm{d}t$ or the region of solid lines is mainly distributed upstream of the vorticity centre; however, the net value of $\mathrm{d}E/\mathrm{d}t$ over the (r, z)-plane is negative according to figure 15(*a*) while in the vortex stretching stage, when $t = 16$ or 22 for example, the net value of $\mathrm{d}E/\mathrm{d}t$ is positive. It is also noticed that during the stage of vortex stretching, i.e. $t = 16$ or 22 in figure 15(*b*), the region which has negative contribution to $\mathrm{d}E/\mathrm{d}t$ or the region of dotted lines is almost separated into two parts by the region having positive contribution. There is one located right next to the colliding surface or $z = 0$ and the other located far from the colliding surface. In order to have a clear view of the weighting associated with these two regions of the negative contribution, we separate them into region I and region II by drawing a horizontal line passing through the centre of the region of positive contribution as shown in figure 15(*b*). Note that the

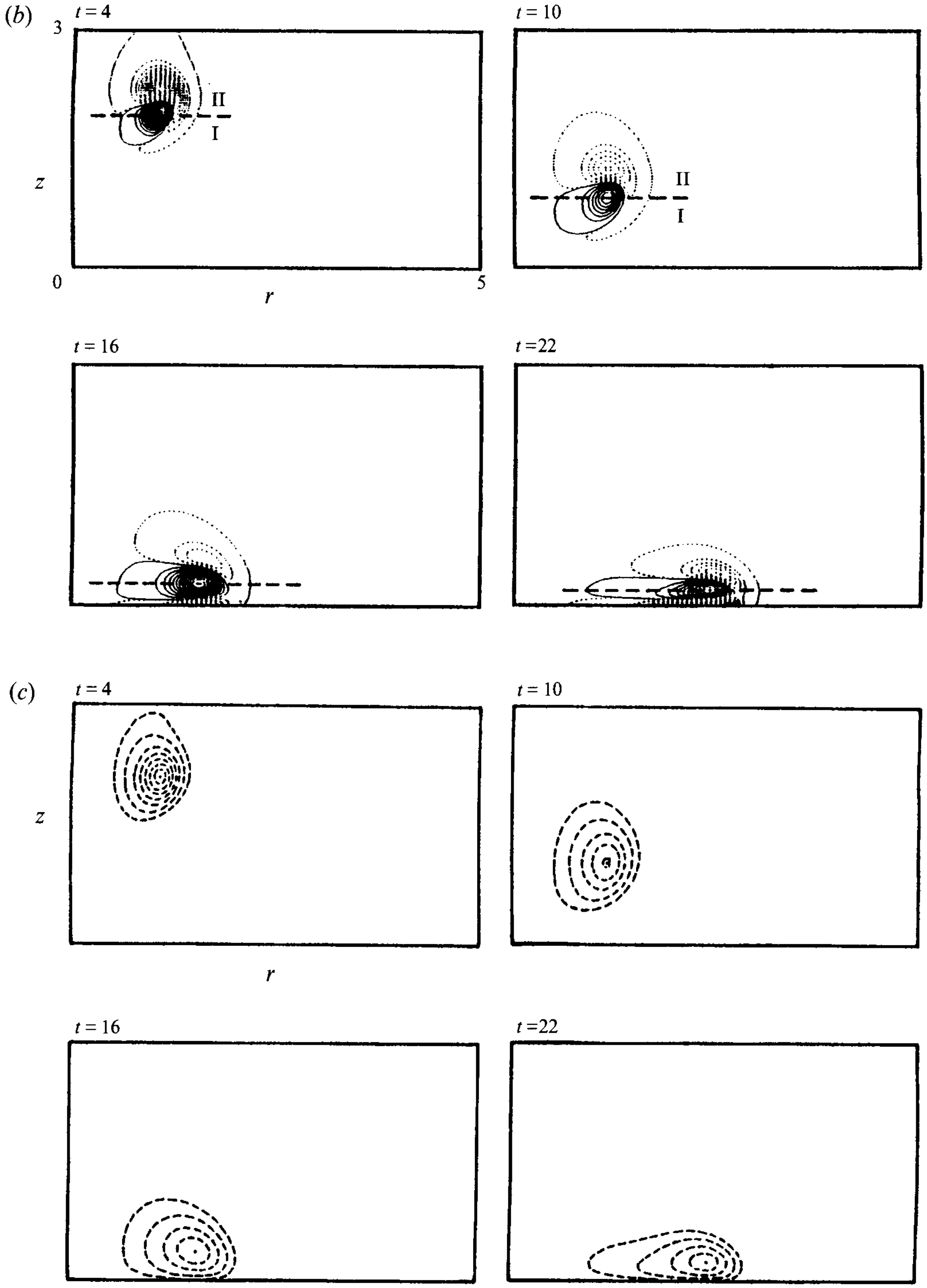

FIGURE 15 (*b*, *c*). For caption see facing page.

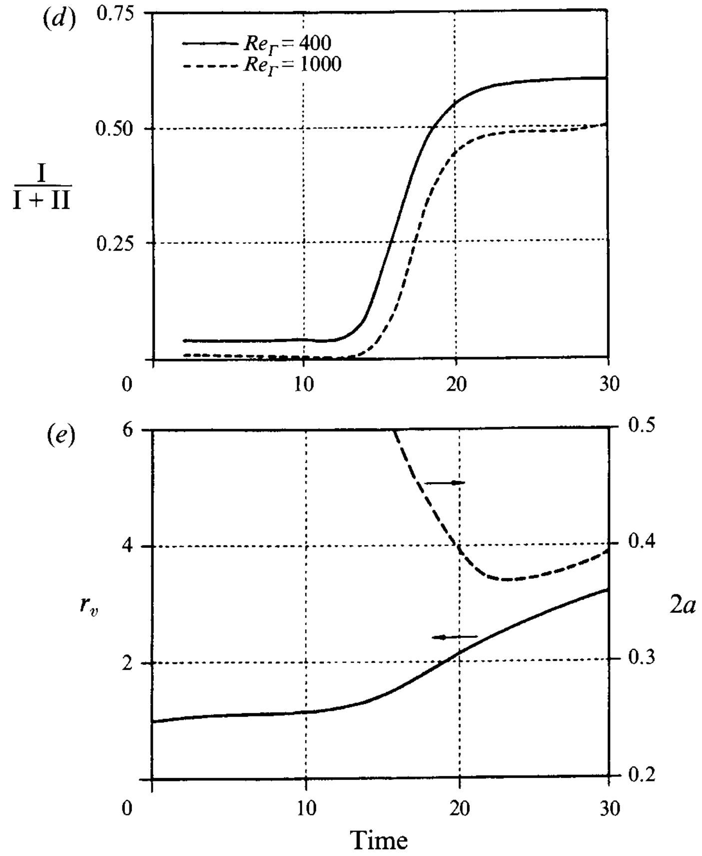

FIGURE 15. Calculated result for $Re_\Gamma = 400$ with $c_0 = 0.20$ and $s_0 = 6$: (*a*) the evolution of the total enstrophy, E, and its time variation, $\mathrm{d}E/\mathrm{d}t$, where the effects of vortex stretching as well as of viscous dissipation on $\mathrm{d}E/\mathrm{d}t$ are also presented in the figure; (*b*) contours of equimagnitude of the integrand shown on the right-hand side of (4.2) at various times, where solid lines represent positive values, and dotted lines represent negative values; (*c*) contours of equivorticity lines for various time values; (*d*) the time evolution of the weighting associated with the ratio of region I to the total negative contribution to $\mathrm{d}E/\mathrm{d}t$, region (I + II); and (*e*) the time evolution of the radius of vortex ring, r_v, as well as the vorticity core diameter, $2a$.

centre of the region of positive contribution is not coincident with that of the vorticity centre as indicated in figure 15(*b*, *c*). Figure 15(*d*) shows the time evolution of the weighting associated with the ratio of region I to the total negative contribution to $\mathrm{d}E/\mathrm{d}t$, i.e. I/(I + II). It is seen in figure 15(*d*), for $t = 16$, that the negative contribution to $\mathrm{d}E/\mathrm{d}t$ associated with region I has about 30% to the total negative contribution while the magnitude of I/(I + II) goes up as time increases. Finally, in the stage of dominance of viscous dissipation, i.e. $t > 19$, the magnitude of I/(I + II) almost reaches an asymptote, which is about 0.6 for $t \approx 22$ as indicated by figure 15(*d*). For $Re_\Gamma = 1000$ with $c_0 = 0.20$, a similar trend of the change of I/(I + II) is also observed in figure 15(*d*), and the vorticity centre is at the closest location to the plane of symmetry when $t \approx 26$ according to figure 14(*b*). Apparently, in the stage of dominance of viscous dissipation, the majority of the contribution to the dissipation of enstrophy is concentrated in the narrow region right next to the colliding surface or the plane of symmetry resulting from large vorticity gradients across the plane of symmetry, $\partial\omega/\partial z$, as shown in figure 15(*c*). In addition, it is also found in figure 15(*a*) that the rebound phenomenon occurs close to the occasion when a local minimum of the variation of enstrophy, dE/dt, is reached in the stage of dominance of viscous dissipation. In other words, the rebound phenomenon occurs at the moment when the effect of viscous dissipation on dE/dt is most significant relative to the effect of vortex stretching.

Furthermore, figure 15(*e*) presents the time evolution of the radius of the vortex ring, r_v, as well as the vorticity core diameter, $2a$, for $Re_\Gamma = 400$, which indicates that the vorticity core diameter, $2a$, reaches its minimum value at $t \approx 23$ and then increases again owing to the dominance of viscous diffusion. This is strong evidence that the vorticity centre which moves apart or rebounds from the plane of symmetry is closely related to the increase of vorticity core diameter owing to severe dissipation of the enstrophy in the region next to the plane of symmetry. Therefore, it may be concluded that the rebound behaviour is essentially a viscous phenomenon in the sense that the effect of viscous dissipation predominates that of vortex stretching.

5. Concluding remarks

Head-on collision of two coaxial vortex rings has been carefully studied by joint experimental and numerical investigation. This joint investigation shows overall agreement, and the main results can be summarized as follows.

(i) The results show that enstrophy, rather than circulation, reveals directly the effects from the vortex stretching and viscous dissipation associated with the three stages of vortex evolution, that is, the free-travelling stage, vortex-stretching stage, and the stage of dominance of viscous dissipation.

(ii) In the stage of free travelling, the circulation of a vortex ring is almost conserved while the enstrophy decreases owing to viscous dissipation.

(iii) The early stage of vortex stretching has been shown to be associated with a sudden increase of enstrophy in the vortex ring and a rapid degradation of circulation between two vortex rings while the stage of viscous dissipation dominance is accompanied by a decrease of enstrophy due to the dominance of viscous dissipation. The analysis also shows that enhancement of the vortical activity of the flow owing to vortex stretching is always accompanied by a speeding up of energy dissipation.

(iv) For higher Re_Γ, the phenomenon of bulging instability around the circumference of a vortex ring has been observed when vortex rings are subjected to stretching during collision. It is found that the occurrence of bulging instability depends on the Reynolds number, Re_Γ, the initial separation of vortex rings, s_0, and the initial core-size of the vortex ring, c_0. A stability map incorporating the three parameters has also been presented based on the experimental observation. Combining the numerical and experimental results show that there exists a threshold or a sufficient condition in N_t/Re_Γ for bulging instability, over which threshold bulging instability will occur. The critical value of N_t/Re_Γ for bulging instability was observed to be larger associated with a vortex ring having a smaller core-size c_0. We also observed a necessary condition associated with the bulging instability; that is, when bulging instability occurred, the lengthscale ratio, $2a/r_v$ was always about 0.06. This verifies that vortex rings with a larger core-size, c_0, or a larger initial value of $2a/r_v$ will need farther stretching in the r-direction when the onset of bulging instability appears. This observation not only enables us to assess the range of validity of the axisymmetry assumed for numerical simulation, but also provides us with a rational basis for further theoretical analysis of azimuthal instability.

(v) The rebound behaviour of vortex rings has been observed in the stage of dominance of viscous dissipation and has been found, indeed, to be related to the increase of vorticity core diameter owing to severe viscous dissipation, when the rate of change of enstrophy reaches a negative minimum with the effect of viscous dissipation predominating that of vortex stretching.

This work was partially supported by the National Science Council, ROC, under contract NSC 81-0401-E002-14. The authors thank Professor Andrew M. Wo in the Institute for his comments and proof-reading of a draft of this paper. We would also like to thank Mr C. T. Chu and Mr H. Y. Liu for their kind assistance in data processing and computer graphics.

REFERENCES

CHU, C. C. & LIAO, Y. Y. 1992 A quantitative study of the flow around an impulsively started circular cylinder. *Exps Fluids* **13**, 137–146.

CHU, C. C., WANG, C. T. & HSIEH, C. S. 1993 An experimental investigation of vortex motions near surfaces. *Phys. Fluids* A **5**, 662–676.

CROW, S. C. 1970 Stability theory for a pair of trailing vortices. *AIAA J.* **8**, 2172–2179.

KAMBE, T. & MINOTA, T. 1983 Acoustic wave radiated by head-on collision of two vortex rings. *Proc. R. Soc. Lond.* A **386**, 277–308.

KAMBE, T. & MYA OO, U. 1984 An axisymmetric viscous vortex motion and its acoustic emission. *J. Phys. Soc. Japan* **53**, 2263–2273.

KHORRAMI, M. R. 1991 On the viscous modes of instability of a trailing line vortex. *J. Fluid Mech.* **225**, 197–212.

LEONARD, A. 1985 Three dimensional vortex flows. *Ann. Rev. Fluid Mech.* **17**, 523–559.

LIM, T. T. & NICKELS, T. B. 1992 Instability and reconnection in the head-on collision of two vortex rings. *Nature* **357**, 225–227.

MAXWORTHY, T. 1972 The structure and stability of vortex rings. *J. Fluid Mech.* **51**, 15–32.

MAXWORTHY, T. 1977 Some experimental studies of vortex rings. *J. Fluid Mech.* **81**, 465–495.

OSHIMA, Y. 1978 Head-on collision of two vortex rings. *J. Phys. Soc. Japan* **44**, 328–331.

PEACE, A. J. & RILEY, N. 1983 A viscous vortex pair in ground effect. *J. Fluid Mech.* **129**, 409–426.

SHARIFF, K., LEONARD, A., ZABUSKY, N. J. & FERZIGER, J. H. 1988 Acoustics and dynamics of coaxial interacting vortex rings. In *Vortex Motion* (ed. H. Hasimoto & T. Kambe), pp. 337–343. North-Holland.

SHARIFF, K. & LEONARD, A. 1992 Vortex rings. *Ann. Rev. Fluid Mech.* **24**, 235–279.

SPALL, R. E., GATSKI, T. B. & GROSCH, C. E. 1987 A criterion for vortex breakdown. *Phys. Fluids* **30**, 3434–3440.

STANAWAY, S., SHARIFF, K. & HUSSAIN, F. 1988 Head-on collision of viscous vortex rings. *Proceedings of the Summer Program, Center for Turbulence Research*, pp. 287–309.

WIDNALL, S. E., BLISS, D. B. & TSAI, C.-Y. 1974 The instability of short waves on a vortex ring. *J. Fluid Mech.* **66**, 35–47.